Epitaxial magnetic van der Waals monolayers on a superconducting substrate

Markus Aapro

School of Science

Thesis submitted for examination for the degree of Master of Science in Technology.

Espoo 29.7.2019

Thesis supervisor:

Prof. Peter Liljeroth

Thesis advisor:

M.Sc. (Tech.) Md Nurul Huda

Aalto University
School of Science

AALTO UNIVERSITY
SCHOOL OF SCIENCE

ABSTRACT OF THE
MASTER'S THESIS

Author: Markus Aapro

Title: Epitaxial magnetic van der Waals monolayers on a superconducting substrate

Date: 29.7.2019 Language: English Number of pages: 7+56

Department of Applied Physics

Degree programme: Engineering Physics (SCI 3056)

Supervisor: Prof. Peter Liljeroth

Advisor: M.Sc. (Tech.) Md Nurul Huda

Topological phases of condensed matter have attracted significant research interest in recent decades. Some of these systems are postulated to support Majorana zero modes, quasiparticle excitations with very attractive properties in terms of topological quantum computing. One proposed system to realize Majorana zero modes involves the interplay of superconductivity and ferromagnetism: when time-reversal symmetry in a superconductor is broken by a magnetic field, the band structure transitions to a non-trivial topological phase, which gives rise to exotic edge states.

To this end, manganese diselenide ($MnSe_2$) islands were grown on a superconducting niobium diselenide ($NbSe_2$) substrate by molecular beam epitaxy. Previous studies have indicated that $MnSe_2$ is a van der Waals -layered material which retains its magnetic properties even in the monolayer limit. Low temperature scanning tunneling microscopy (STM) was used to verify the island growth and measure lattice constants and island heights on the samples. Scanning tunneling spectroscopy (STS) was used to probe the electronic structure of the grown islands.

The topography measurements revealed several distinct phases of $MnSe_x$ layers with average lattice constants of 3.6 Å, 3.8 Å and 4.3 Å, from which the 4.3 Å phase was the most abundant. The islands had collectively aligned atomically sharp edges and exhibited a moiré pattern. No signs of edge states corresponding to Majorana zero modes were observed in the spectroscopy measurements: spectroscopy performed in an applied magnetic field showed that Abrikosov vortices were unaffected by the islands. These results indicate that the grown $MnSe_x$ islands do not support non-trivial topological phases and may not retain their magnetic behaviour in the monolayer limit. *In situ* surface composition measurements and better control over growth parameters would be required to investigate the island formation further.

Keywords: Scanning tunneling microscopy, tunneling spectroscopy, superconductivity, magnetism, Majorana zero mode

AALTO-YLIOPISTO
PERUSTIETEIDEN KORKEAKOULU

DIPLOMITYÖN
TIIVISTELMÄ

Tekijä: Markus Aapro

Työn nimi: Suuntautuneet magneettiset van der Waals -yksittäiskerrokset suprajohtavalla pinnalla

Päivämäärä: 29.7.2019 Kieli: Englanti Sivumäärä: 7+56

Teknillisen fysiikan laitos

Koulutusohjelma: Teknillinen fysiikka (SCI 3056)

Työn valvoja: Prof. Peter Liljeroth

Työn ohjaaja: DI Md Nurul Huda

Topologiset faasit ovat viime vuosikymmenten aikana herättäneet runsaasti mielenkiintoa tiiviin aineen tutkimuksessa. Tiettyjen topologisten hilojen on ennustettu synnyttävän niin kutsuttuja Majorana-nollamoodeja: kvasihiukkasia, joilla on erittäin lupaavia ominaisuuksia topologisen kvanttilaskennan kannalta. Näitä nollamoodeja on ennustettu syntyvän systeemeissä, joissa suprajohde ja ferromagneetti vuorovaikuttavat keskenään: kun magneettikenttä rikkoo aikasymmetrian suprajohteessa, hilan vyörakenne muuttuu ja topologisia reunatiloja odotetaan syntyvän.

Tällaisten systeemien tutkimiseksi tässä diplomityössä kasvatettiin mangaanidiselenidi-saarekkeita ($MnSe_2$) suprajohtavalle niobiumdiselenidi-substraatille ($NbSe_2$). Aiempien tutkimusten mukaan $MnSe_2$ muodostaa van der Waals -voimilla sitoutuneita kerrosrakenteita ja pysyy magneettisena jopa yksittäisenä molekyylikerroksena. Matalan lämpötilan tunnelointimikroskopialla vahvistettiin saarekkeiden suuntautunut kasvu ja selvitettiin näytteiden hilavakioita sekä saarekkeiden korkeuksia. Lisäksi näytteiden elektronista rakennetta tutkittiin tunnelointispektroskopialla.

Topografia-mittaukset paljastivat useita erillistä $MnSe_x$-faaseja, joiden keskimääräiset hilavakiot olivat 3.6 Å, 3.8 Å ja 4.3 Å. Atomitasolla teräväreunaiset saarekkeet muodostuivat suuntautuneesti suhteessa pintakerrokseen ja saarekkeilla havaittiin moiré-kuvioita. Majorana-nollamoodeihin liittyviä reunatiloja ei havaittu spektroskopia-mittauksissa. Lisäksi ulkoisessa magneettikentässä tehty spektroskopia paljasti, etteivät saarekkeet vaikuttaneet pinnan Abrikosov-pyörteisiin. Tulosten perusteella kasvatetut $MnSe_x$-saarekkeet eivät tue topologisia faaseja eivätkä välttämättä pysy magneettisina yksittäisinä molekyylikerroksina. Saarekkeiden kasvun yksityiskohtaisempi tutkimus edellyttäisi pinnan kemiallisen koostumuksen *in situ*-mittauksia sekä parempaa kasvatusparametrien hallintaa.

Avainsanat: Tunnelointimikroskopia, tunnelointispektroskopia, suprajohde, magnetismi, Majorana-nollamoodi

Acknowledgements

On an August evening in 2009, a kid in Kilkenny, Ireland, buys a book that changes the course of his life. Roughly ten years later he lays down a book of his own making. This, however, would have been impossible without the help of some extraordinary people.

Firstly, I would like to thank my supervisor Professor Peter Liljeroth for continuous support over the years and especially during the making of this thesis. Peter's front-line leadership and critical insight were instrumental in steering the process. I am grateful to my advisors Md Nurul Huda and Shawulienu Kezilebieke for all the experimental support and limitless patience towards my questions. Special thanks to Somesh Ganguli for the spectroscopy measurements and theoretical discussions, and to Jani Sainio for valuable advice on experimental issues. The Atomic Scale Physics group has been a great team to work with: many thanks to the past and present members for Cake, lunch company and all the discussions. With a crew like this, I expect great things to emerge when we dive deeper into the Fermi sea.

This thesis also marks the end of my student life, which has been quite the ride indeed. Many thanks to the Guild of Physics for providing an extraordinary community and making people venture into the improbable. Special thanks to Raati 16 for the shared work and pleasures, and to Fyysikkospeksi for doing the impossible on a regular basis. I feel grateful and fortunate to have met and become friends with so many exceptional people during my years in Otaniemi: many thanks to all of you.

I have had the privilege of working multiple summers at the Department of Applied Physics: many thanks to the past and present members of the Nanomaterials Group for letting me work on carbon nanotubes and gain experience in experimental research. I also thank Taru Bister, Professor Mikko Alava and many others for fruitful correspondence on teaching-related issues and academic affairs.

Lastly, I would like to thank the people who have stood by me through these past six years and more. My high-school friends have been a constant source of support and joy, as have my oldest friends Anssi and Samppa. Many thanks to all the relatives and friends of our family. Finally, I thank my mom and dad for all the support, encouragement and love that have kept me going through the hard times.

I dedicate this thesis to my grandfather Ilmari Aapro, who never had the chance to study in his youth. His example shows that the path to wisdom can have the humblest of beginnings.

Otaniemi, July 29, 2019

Markus Aapro

Contents

Abbreviations

2D	Two-dimensional
BCS	Bardeen-Cooper-Schrieffer
CDW	Charge density wave
CVD	Chemical vapor deposition
dI/dV	Differential conductance
GL	Ginzburg-Landau theory
HOPG	Highly oriented pyrolytic graphite
IS	Inversion symmetry
LDOS	Local density of states
MBE	Molecular beam epitaxy
MZM	Majorana zero mode
QHE	Quantum Hall effect
SNS	Superconductor - normal conductor - superconductor
SPT	Symmetry protected topological phase
STM	Scanning tunneling microscopy
STS	Scanning tunneling spectroscopy
TMD	Transition metal dichalcogenide
TRS	Time reversal symmetry
vdW	van der Waals
YSR	Yu-Shiba-Rusinov

1 Introduction

The introduction of novel forms of mathematics has been the driving force behind many groundbreaking discoveries in physics. One relatively recent example is the introduction of topological concepts in condensed matter physics. Berezinskiĭ, Kosterlitz and Thouless applied the formalism of topology to explain a new type of phase transition which did not involve spontaneous symmetry breaking [1, 2]. Topological materials have received wide-spread research interest in recent decades, and their potential applications range from quantum computing to spintronics and dissipationless electronics [3, 4].

A particular type of topological excitations share characteristics with the elusive Majorana fermion: these Majorana zero modes (MZMs) have been predicted to obey a wider range of exchange statistics than conventional bosons and fermions. MZMs are expected to emerge at the interstice of superconducting and ferromagnetic systems: the competition between the mutually exclusive spin coupling types result in the emergence of topological edge states. Access to MZMs would be a major step towards topological quantum computing as well as enabling a host of novel experiments on condensed matter physics. The short-range interactions between superconductors and magnets are a recurring problem in experimental studies of MZMs: placing a magnetic impurity into a superconducting lattice suppresses the magnetism of the impurity, and vice versa. Recent advances in two-dimensional (2D) materials offer a solution to this problem in the form of van der Waals (vdW) crystals, some of which have been shown to support ferromagnetism and superconductivity down to the monolayer limit [5]. These materials also have interesting properties in their own right: 2D magnetic materials enable various experiments on fundamental theories of magnetism and potential applications in spintronics.

This thesis is an experimental study on the epitaxial growth of magnetic manganese diselenide ($MnSe_2$) islands on a superconducting niobium diselenide ($NbSe_2$) substrate. Molecular beam epitaxy (MBE) was used to grow samples, which were analysed with low temperature scanning tunneling microscopy (STM). The electronic properties of the island-surface systems were studied by scanning tunneling spectroscopy (STS). Various phases of 2D $MnSe_x$ were identified and studied. Despite the absence of edge states associated with MZMs, the obtained results included unexpected findings (including a moiré pattern) and pave the way for computational studies of these exotic materials.

The background chapter introduces the reader to the fundamentals of topology in condensed matter, superconductivity in the presence of magnetic impurities and the growing family of magnetic 2D vdW crystals. The experimental methods chapter explains the physical principles and operation of STM and spectroscopy in addition to summarizing the MBE setup. The results of topographic and spectroscopic measurements are provided in the following chapter, highlighting the primary findings in the various samples. Finally, a summary chapter closes the discussion and proposes further experiments on the interplay of superconductivity and magnetism in 2D systems.

2 Background

This section summarizes the essential theoretical and experimental background regarding the coexistence of magnetism and superconductivity in 2D systems. The background also provides motivation for the specific experiments performed in this thesis. First, a short introduction to topology in condensed matter is provided from the viewpoint of experimental physics. After this we proceed to discuss superconductivity in the presence of magnetic impurities and how these systems relate to topological phenomena. The section concludes with a discussion on how to test these theories with novel 2D magnetic materials.

2.1 Topological phases in condensed matter

Topology as a branch of mathematics is the study geometrical objects and manifolds that share some invariant properties under continuous deformations. The mathematical formalisms developed in topology have also found their use in condensed matter physics, where topological order can explain phase transitions which do not involve spontaneous symmetry breaking [1, 2]. Although Landau's symmetry-based theory of phase transitions is widely applicable [6], recent research has unveiled a host of phenomena that cannot be explained without the introduction of topological concepts. These include the different varieties of quantum Hall effects (QHE), topological insulators, topological superconductors and various edge states. Materials with topology-induced properties have also been proposed as potential platforms of quantum computation, which has become a major research motivator [4].

Phases that comply with Landau's theory of phase transitions are called topologically trivial, whereas other states of matter are called topologically non-trivial. The quasiparticles associated with the latter, such as edge states, exhibit certain distinctive features. Firstly, topological phases may exhibit anyonic exchange statistics as opposed to fermionic or bosonic ones. This means that when quasiparticles corresponding to a topological phase exchange positions, the resulting wave function may change by an arbitrary phase θ (for fermions $\theta = \pi$ and for bosons $\theta = 0$, see figure 1). The anyon statistics are called Abelian if the real part of the wave function remains unchanged by the exchange operation. For non-Abelian statistics, the exchange operation moves the system from one degenerate ground state to another, changing both the complex phase and the real part of the wave function [7]. This property could theoretically be exploited to propagate quantum information in a topological quantum computer.

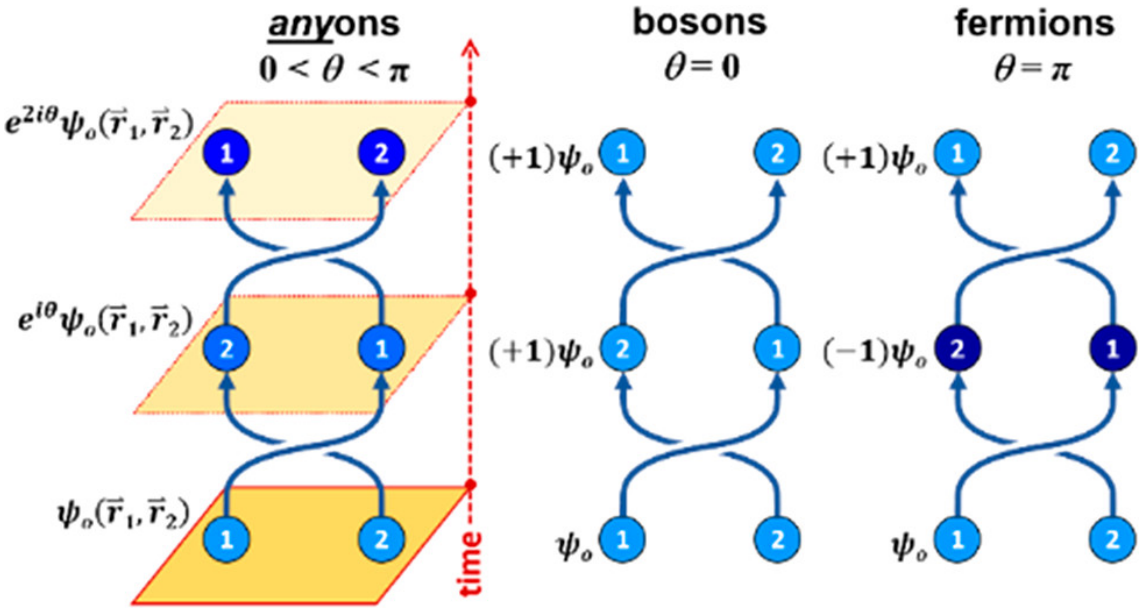

Figure 1: Exchange operations on Abelian anyons, bosons and fermions initially in state ψ_0. Wave function phase is denoted by particle colour brightness. For bosons and fermions, applying an even number of exchange operations results in the original wave function. For Abelian anyonic quasiparticles the wave function phase changes by $2n\theta$. Image reproduced from [4].

Because topological phases emerge from the properties of the bulk band structure, local deformations of the lattice do not destroy the topological phase. This makes topological phases intrinsically fault tolerant, or topologically protected, against external perturbations, a property very well suited for quantum computation platforms [8]. In other types of quantum computation decoherence causes information losses and fault tolerance can only be achieved through corrective algorithms [9]. Despite their promising features, a complete universal quantum computer cannot be built with topological components alone [3].

Various topological phases can be classified based on the localization of the topological states: some topological phases exist only as edge states, whereas others permeate the bulk lattice. The latter are called intrinsic topological states, some examples being the states associated with various types of QHE. In intrinsic topological states, the quasiparticles can remain correlated over a long distance, whereas in edge states corresponding to so called symmetry protected topological (SPT) phases the correlation range is smaller. Examples of SPT phases include topological insulators, topological superconductors and topological semi-metals [3]. These materials are of particular interest in surface science, where the boundaries of bulk crystals are exposed for investigation. Figure 2 lists the various SPT and intrinsic topological phases of quantum matter.

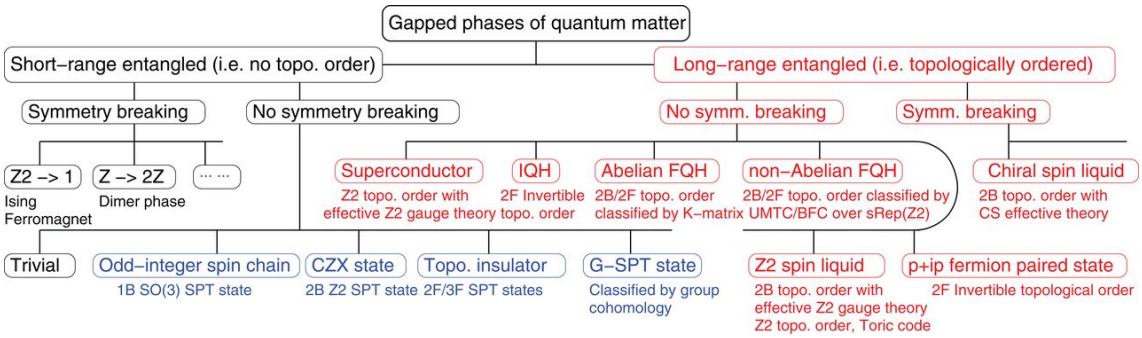

Figure 2: A tree-chart representing the various states of quantum matter, with SPT phases on blue and intrinsic topological phases on red. Image reproduced from [3].

2.1.1 Topological invariants: Chern number and $\mathbb{Z}_2$ invariant

In topology, shapes and objects are classified in terms of integer constants that remain invariant under continuous deformations. For instance, a coffee cup and a doughnut are topologically equivalent since they share a genus value one, whereas a pair of pants (of finite thickness) has a genus value two (in layman terms, genus equals the number of 'handles' on an object). In condensed matter physics, topological invariants acquire non-zero values for topologically non-trivial phases.

Topological phases of quantum matter can be classified in terms of two topological invariants called the Chern number and the $\mathbb{Z}_2$ invariant. These are defined in terms of Berry connection and Berry curvature in $\mathbf{k}$-space. By considering a crystalline solid with translational symmetry, as discussed by Weng et al. [10, 11], the Schrödinger equation in real space basis can be written as

$$\hat{H}(\mathbf{r})\psi_{n\mathbf{k}}(\mathbf{r}) = \epsilon_{n\mathbf{k}}\psi_{n\mathbf{k}}(\mathbf{r}), \tag{1}$$

where n is the band index. Translational symmetry makes the system $\mathbf{k}$-dependent in the first Brillouin zone. By applying Bloch's theorem

$$\psi_{n\mathbf{k}}(\mathbf{r}) = e^{i\mathbf{k}\cdot\mathbf{r}}u_{n\mathbf{k}}(\mathbf{r}), \tag{2}$$

the Schrödinger equation can be recast in terms of the periodic Bloch wave functions $u_{n\mathbf{k}}(\mathbf{r})$ as

$$\hat{H}(\mathbf{r})_{\mathbf{k}}u_{n\mathbf{k}}(\mathbf{r}) = \epsilon_{n\mathbf{k}}u_{n\mathbf{k}}(\mathbf{r}), \tag{3}$$

where the Hamiltonian

$$\hat{H}(\mathbf{r})_{\mathbf{k}} = e^{-i\mathbf{k}\cdot\mathbf{r}}\hat{H}(\mathbf{r})e^{i\mathbf{k}\cdot\mathbf{r}}. \tag{4}$$

In this basis, an overlap of two eigenfunctions separated by an infinitesimal $\mathbf{k}$-space element $\Delta\mathbf{k}$ can be evaluated as

$$\langle u_n(\mathbf{k})|u_n(\mathbf{k}+\Delta\mathbf{k})\rangle = 1 + \Delta\mathbf{k}\,\langle u_n(\mathbf{k})|\,\nabla_{\mathbf{k}}\,|u_n(\mathbf{k})\rangle = e^{-i\Delta\mathbf{k}\cdot\mathbf{A}_n(\mathbf{k})}, \tag{5}$$

where

$$\mathbf{A}_n(\mathbf{k}) = i \langle u_n(\mathbf{k}) | \nabla_{\mathbf{k}} | u_n(\mathbf{k}) \rangle \tag{6}$$

is the Berry connection, which is gauge dependent and as such non-observable. Berry connection can be viewed as an effective vector potential in **k**-space, so the curl

$$\Omega_n(\mathbf{k}) = \nabla_k \times \mathbf{A}_n \tag{7}$$

also known as Berry curvature corresponds to an effective magnetic field in **k**-space. Berry curvature can in turn be integrated over a closed loop C to obtain the Berry phase γ_n, a magnetic flux analogue defined as

$$\gamma_n = \oint_C \mathbf{A}_n(\mathbf{k}) \cdot d\mathbf{k} = \int_S \Omega_n(\mathbf{k}) d\mathbf{S}, \tag{8}$$

where S is the surface enclosed by $C = \partial S$. By imposing periodic boundary conditions on the Bloch states $u_n(\mathbf{k})$ in **k**-space, the 2D Brillouin zone becomes equivalent to a torus (complete rotations through the 'hole' and along the edge of the torus lead to the original **k**-space point). In such a geometry, Chern's theorem dictates that the Berry phase becomes an integer multiple of 2π, where the integer

$$Z = \frac{1}{2\pi} \int_S \Omega_n(\mathbf{k}) d\mathbf{S} \tag{9}$$

is the Chern number [12]. In the case of 2D Chern insulators, where the Hall conductivity of the material is quantized as $\sigma_{xy} = -\frac{e^2}{h} Z$, the Chern number is equal to the number of edge states in the system [10].

The bulk symmetries of a system have direct implications on the Berry curvature and consequently on the topological invariants. In particular, inversion symmetry (IS) and time reversal symmetry (TRS) can be expressed in terms of the following boundary conditions:

$$\begin{aligned} \Omega_n(\mathbf{k}) &= \Omega_n(-\mathbf{k}) \quad \text{for IS} \\ \Omega_n(\mathbf{k}) &= -\Omega_n(-\mathbf{k}) \quad \text{for TRS} \end{aligned} \tag{10}$$

Applying both of these relations at once results in $\Omega_n(\mathbf{k}) = 0$, and thus a trivial topology of the band structure. This highlights the fact that topological phases are typically localized to edges of domains where either TRS or IS is broken. Examples of these include vortex cores in superconductors [13], where TRS breaks due to spin-orbit coupling, and inversion asymmetric topological insulators [14].

The necessity of a second topological invariant besides the Chern number, namely the $\mathbb{Z}_2$ invariant, arises by considering 2D insulators with TRS. This results in a vanishing Chern number, but not necessarily to trivial topological properties as shown by Kane and Mele [15]. By considering only the positive half plane of the Brillouin zone (B^+), the topological properties of a 2D band insulator can be characterized by

$$\mathbb{Z}_2 = \frac{1}{2\pi} \left(\oint_{\partial B^+} \mathbf{A}(\mathbf{k}) \cdot d\mathbf{k} - \int_{B^+} \Omega_z(\mathbf{k}) d^2\mathbf{k} \right) \bmod 2, \tag{11}$$

where $\mathbf{A}(\mathbf{k})$ is the Berry connection and $\Omega_z(\mathbf{k})$ is the Berry curvature. Several alternative definitions for the $\mathbb{Z}_2$ invariant can also be formulated [16]. The edge states corresponding to a non-zero value of $\mathbb{Z}_2$ always appear in counter-propagating pairs due to the TRS [10]. The number of these edge state pairs modulo 2 corresponds to the $\mathbb{Z}_2$ value.

An exhaustive classification of topological insulators and topological superconductors is given by the 'ten-fold way' described by Altland and Zirnbauer [17]. They showed that systems involving time-reversal symmetry, particle-hole symmetry and/or chiral symmetry can be classified into ten unique symmetry classes. The symmetries can either be present, broken or, in the case of time-reversal and particle-hole symmetries, an antisymmetry may exist. Each symmetry class can be applied to bulk band structures to predict whether or not non-trivial topology emerges and what is the relevant topological invariant [18]. Table 1 illustrates the ten-fold way in three dimensions. The symmetry classes are denoted according to the symmetric space classification by Élie Cartan [19].

Table 1: The 'ten-fold way' in three dimensions [20]. $\mathcal{T}$, $\mathcal{C}$ and $\mathcal{S}$ refer to time reversal, particle-hole and chiral symmetries, respectively, and their values correspond to absence (0), presence (1) and antisymmetry (-1). The symmetry groups corresponding to non-trivial topology in 2D are highlighted.

	Symmetries			Dimension		
Cartan label	$\mathcal{T}$	$\mathcal{C}$	$\mathcal{S}$	1	2	3
A	**0**	**0**	**0**	0	$\mathbb{Z}$	0
AIII	0	0	1	$\mathbb{Z}$	0	$\mathbb{Z}$
AI	1	0	0	0	0	0
BDI	1	1	1	$\mathbb{Z}$	0	0
D	**0**	**1**	**0**	$\mathbb{Z}_2$	$\mathbb{Z}$	0
DIII	**-1**	**1**	**1**	$\mathbb{Z}_2$	$\mathbb{Z}_2$	$\mathbb{Z}$
AII	**-1**	**0**	**0**	0	$\mathbb{Z}_2$	$\mathbb{Z}_2$
CII	-1	-1	1	$\mathbb{Z}$	0	$\mathbb{Z}_2$
C	**0**	**-1**	**0**	0	$\mathbb{Z}$	0
CI	1	-1	1	0	0	$\mathbb{Z}$

2.2 Superconductivity and magnetic impurities

Three years after H. Kamerlingh Onnes successfully liquefied helium for the first time in 1908, he found that mercury loses its electrical resistivity below a critical temperature [21]. Later experiments by Meissner and Ochsenfeld found that in this state of perfect conductivity no magnetic field permeates the conductor [22]. Materials with these two properties, namely perfect electrical conductance and perfect diamagnetism, are called superconductors. During the past hundred years, intense research effort has been directed into explaining the emergence of the superconducting state and realising superconductivity in increasingly complex crystal structures. The notion of topological phases has also been successfully applied to superconducting

systems.

Superconductors are primarily classified by their critical temperatures, their magnetic field responses and their compliance with the Bardeen-Cooper-Schrieffer (BCS) theory. If a material becomes superconducting at a temperature above 30 K, it is considered a high-temperature superconductor. This was thought to be impossible within the BCS framework until Bednorz and Müller found a perovskite material with a critical temperature above 30 K [23]. Another critical phase transition in superconductors occurs when it is subjected to a magnetic field. In type I superconductors, the superconductivity vanishes instantly when a material specific critical field strength is exceeded. In a type II superconductor, the transition occurs in two stages: localized vortices of normal conductivity appear when the field strength lies between two critical values [24].

2.2.1 Macroscopic theory: London, Ginzburg-Landau

The theory of superconductivity has been formulated in both macroscopic and microscopic contexts. The first theoretical treatise of superconducting phenomena was given by London and London [25], who discussed the Meissner effect (i.e. perfect diamagnetism) in superconductors. The London model is based on some electrons moving freely in a superconductor, and the rest exhibiting the Ohmic resistance of normal conductors [21]. They formulated a characteristic length scale called London penetration depth, which defines the extent by which a magnetic field permeates a superconductor. The penetration depth is shown to be temperature dependent by approximately

$$\lambda_L(T) \approx \frac{\lambda(0)}{\sqrt{1-(T/T_c)^4}}, \tag{12}$$

where T_c is the critical temperature. A further macroscopic theory was developed by Ginzburg and Landau in 1950, which is based on Landau's earlier work on phase transitions due to spontaneous symmetry breaking [26]. The theory is formulated in terms of an order parameter ψ, which attains non-zero values in the broken symmetry phase (i.e. the superconducting state). The free energy of the system can be expressed in terms of the order parameter as

$$F_{GL} = F_n + \alpha|\psi|^2 + \frac{\beta}{2}|\psi|^4 + \frac{1}{2m}\left|\left(-i\hbar\nabla - \frac{2e\mathbf{A}}{c}\right)\psi\right|^2 + \frac{|\mathbf{B}|^2}{2\mu_0}, \tag{13}$$

where F_n is the free energy of the normal state, α and β are phenomenological constants and $\mathbf{A}$ is the magnetic vector potential. The order parameter ψ is a complex quantity related to the number density of superconducting electrons. By minimizing the free energy with respect to the order parameter and the vector potential we arrive at the Ginzburg-Landau equations [27]

$$\alpha\psi + \beta|\psi|^2\psi + \frac{1}{2m}\left(-i\hbar\nabla - 2e\mathbf{A}\right)^2\psi = 0 \tag{14a}$$

$$\nabla \times \mathbf{B} = \mu_0\mathbf{j} = \mu_0\frac{2e}{m}\,\mathrm{Re}\{\psi^*\left(-i\hbar\nabla - 2e\mathbf{A}\right)\psi\}, \tag{14b}$$

where * denotes complex conjugation. The spatial variation of the order parameter introduces a new characteristic length scale called coherence length. For instance, in a one-dimensional system without magnetic field equation 14a becomes

$$-\frac{\hbar^2}{2m}\frac{\partial^2\psi}{\partial x^2} + \alpha\psi + \beta\psi^3 = 0. \tag{15}$$

In equilibrium the order parameter magnitude is defined by the coefficients α and β as

$$|\psi_0|^2 = \Delta_{GL}^2 = \frac{-\alpha}{\beta} > 0. \tag{16}$$

By assuming small perturbations from the equilibrium, the order parameter in equation 15 can be expressed as $\psi = \psi'\Delta_{GL}$ [26]. The recast equation becomes

$$\begin{aligned} &-\frac{\hbar^2}{2m}\frac{\partial^2\psi'}{\partial x^2} + \alpha\psi' + \beta\Delta_{GL}^2|\psi'|^2\psi' = 0 \\ \Leftrightarrow\ &-\frac{\hbar^2}{2m}\frac{\partial^2\psi'}{\partial x^2} + |\alpha|\left(|\psi'|^2 - 1\right)\psi' = 0. \end{aligned} \tag{17}$$

Thus we find the coherence length

$$\xi^2 = \frac{\hbar^2}{2m|\alpha|}, \tag{18}$$

which defines the spatial variation of the order parameter close to equilibrium. Higher dimensional superconductors may exhibit different coherence lengths in different lattice directions. Analysing the sign of the coefficient α on both sides of the superconducting phase boundary and deriving the penetration depth in terms of the GL theory leads to the same temperature dependence for ξ and λ_L [26]. Thus the ratio

$$\kappa = \frac{\lambda_L(T)}{\xi(T)} = \frac{mc}{2e\hbar}\sqrt{\frac{\beta}{2\pi}}, \tag{19}$$

called the Ginzburg-Landau parameter, is a dimensionless temperature invariant constant.

2.2.2 Proximity effect

As discussed by London and London, there is a finite length scale over which magnetic fields can penetrate a superconductor, resulting in regions of normal conductivity. The inverse of this phenomenon also exists: the Cooper pairs of a superconductor

can permeate into normal conductors, leading to local superconductivity in materials which do not support it intrinsically. This proximity effect was discovered in 1937 by Holm and Meissner, who studied superconductor-normal conductor-superconductor (SNS) junctions and found that the junction carries supercurrent when the normally conducting layer is sufficiently thin [28]. The order parameter and thus the energy gap of the proximity-induced superconductor decays exponentially with distance from the superconductor, but for some materials, like copper, the Cooper pairs can permeate thousands of Ångströms into the normal conductor [29]. The proximity range of the Cooper pairs also depends on the Fermi velocity of the material: for insulators the range is smaller than for normal conductors [26].

A proximity-induced gap can also exist in ferromagnetic materials [30], where the mutually exclusive spin coupling of Cooper pairs and ferromagnetic lattices causes oscillations in the order parameter. A schematic of the order parameter decay in normal metals and ferromagnets in presented in figure 3. Recent research has also suggested that Cooper pairs in proximity-induced superconductors can exhibit spin triplet pairing ($S = 1$) as opposed to the conventional singlet pairing ($S = 0$) [31, 32].

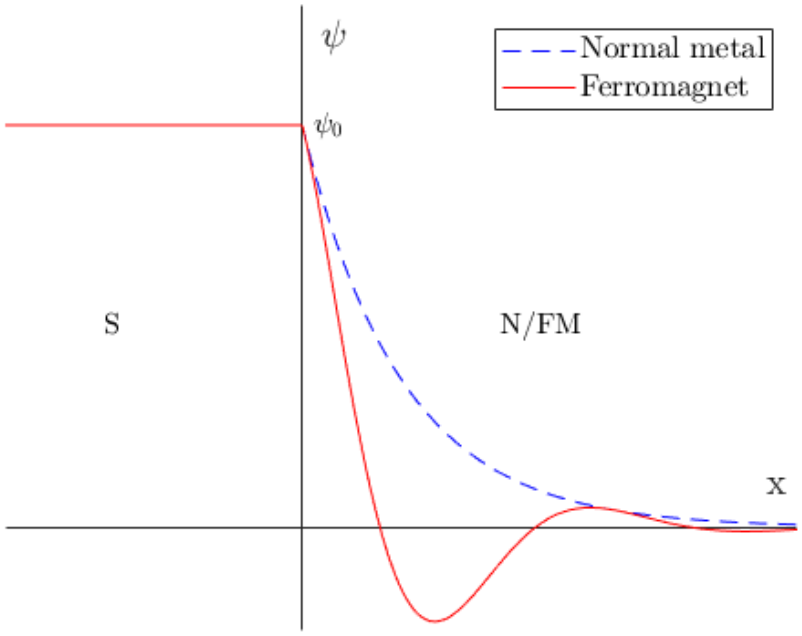

Figure 3: Schematic of the GL order parameter decay in a normal metal and a ferromagnet [33]. ψ_0 denotes the order parameter value close to the superconducting junction and distance x is perpendicular to the junction. The spin-coupling of the ferromagnet and Cooper pairs causes oscillations in the order parameter.

2.2.3 Microscopic theory: BCS, Bogoliubov-de Gennes

After decades of work on the macroscopic description of superconductivity, a successful microscopic theory was finally developed by Bardeen, Cooper and Schrieffer in 1957 [34]. For this contribution the authors were awarded the Nobel Prize in Physics in 1972. BCS theory presents the emergence of a superconducting state as the result of an attractive potential between individual electrons. The attractive interaction between these Cooper pairs of electrons is mediated by virtual phonons, which dominate the electron-electron interactions close to the Fermi level below the critical temperature. Once an attractive interaction between electrons is established, however small it may be, the electrons will keep forming Cooper pairs until pair formation becomes energetically unfavorable. Thus the electronic states close to the Fermi level disappear within a certain energy gap inside which Cooper pairing is favorable. The Cooper pairs condense like bosons to form a single macroscopically delocalized quantum state spanning across the superconductor.

A key result of the BCS theory is the following expression for a superconducting density of states (DOS)

$$\rho(E) = \begin{cases} \frac{E}{\sqrt{E^2-\Delta^2}}, & |E| > \Delta \\ 0, & |E| \leq \Delta, \end{cases} \tag{20}$$

where Δ is a material specific superconducting gap corresponding to the energy required to break a Cooper pair. The real part of the Ginzburg-Landau order parameter can be shown to correspond to the BCS energy gap, and expressions for the phenomenological parameters α and β can also be derived. Superconductors which exhibit an LDOS similar to equation 20 are called conventional, the others being unconventional. Figure 4 shows a schematic of the BCS LDOS.

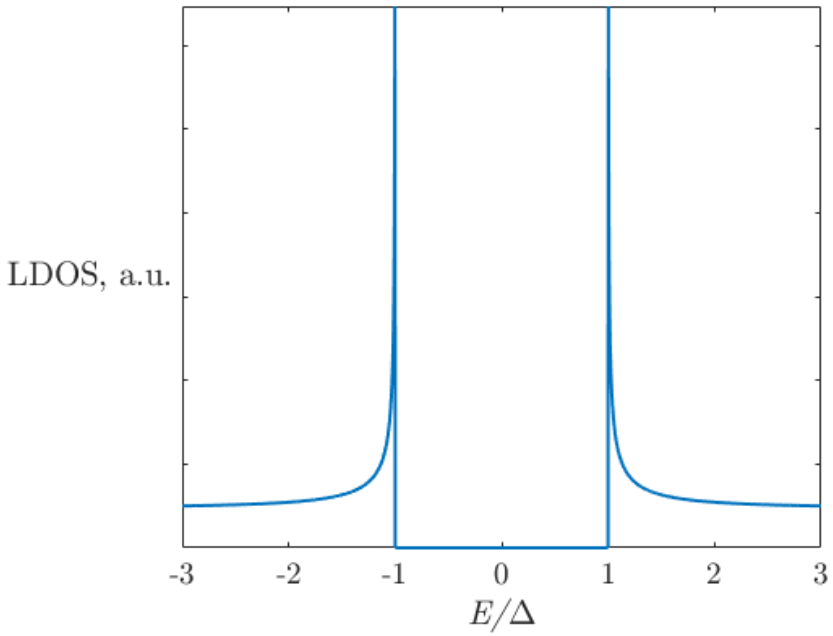

Figure 4: A plot of the BCS LDOS as given in equation 20. The abrupt change in LDOS close to the gap energy can be exploited in tunneling experiments requiring high energy resolution.

The BCS theory can be extended to account for non-uniform superconductors with impurities, boundary effects etc. as shown by Bogoliubov and de Gennes [35, 36]. A particularly important prediction of the theory is Bogoliubov quasiparticles, which introduce electronic states with a finite lifetime inside the superconducting gap. Various types of impurities can be accounted for by introducing the relevant terms into the Bogoliubov-de Gennes Hamiltonian. In a general form the Bogoliubov-de Gennes equations are given by

$$\begin{aligned} -\frac{\hbar^2}{2m}\left(\nabla - \frac{ie}{\hbar c}\mathbf{A}\right)^2 u_{\mathbf{k}}(\mathbf{r}) + [U(\mathbf{r}) - \mu]\, u_{\mathbf{k}}(\mathbf{r}) + \Delta(\mathbf{r}) v_{\mathbf{k}}(\mathbf{r}) = E_{\mathbf{k}} u_{\mathbf{k}}(\mathbf{r}) \\ \frac{\hbar^2}{2m}\left(\nabla - \frac{ie}{\hbar c}\mathbf{A}\right)^2 v_{\mathbf{k}}(\mathbf{r}) - [U(\mathbf{r}) - \mu]\, v_{\mathbf{k}}(\mathbf{r}) + \Delta(\mathbf{r})^* u_{\mathbf{k}}(\mathbf{r}) = E_{\mathbf{k}} v_{\mathbf{k}}(\mathbf{r}), \end{aligned} \tag{21}$$

where $U(\mathbf{r})$ is an external scalar potential, μ is the chemical potential, $\Delta(\mathbf{r})$ is the energy gap and $u_{\mathbf{k}}(\mathbf{r})$ and $v_{\mathbf{k}}(\mathbf{r})$ are creation operators for electron- and hole-like quasiparticle states respectively. The operators $u_{\mathbf{k}}(\mathbf{r})$ and $v_{\mathbf{k}}(\mathbf{r})$ are symmetrically normalized as

$$|u_{\mathbf{k}}(\mathbf{r})|^2 + |v_{\mathbf{k}}(\mathbf{r})|^2 = 1. \tag{22}$$

2.2.4 Magnetic impurities on a superconducting surface

Superconductors in the presence of magnetic impurities are of particular interest in the context of topological phases. As discussed in the previous section, magnetism

and superconductivity do not mix well: an increase in magnetic field brings the superconductor closer to its normal state, or destroys the superconductivity entirely. Magnetic impurities also cause a more subtle change in the band structure of the superconductor by locally breaking the TRS. This leads to the possibility of non-trivial topological phases in magnetic impurity lattices [37].

In the Bogoliubov-de Gennes formalism a magnetic impurity is expected to induce quasiparticle states inside the superconducting gap. The properties of these states were studied in detail by Yu, Shiba and Rusinov (YSR) [38, 39, 40] and recently their presence has been experimentally verified in various systems [41, 42]. The energies and lifetimes of the YSR states are strongly dependent on the exchange coupling between the impurity and the superconducting substrate, which depends on the specific adsorption configuration of the impurity [41]. Figure 5 shows tunneling spectra of individual and coupled magnetic cobalt phthalocyanine (CoPC) molecules measured with a superconducting tip.

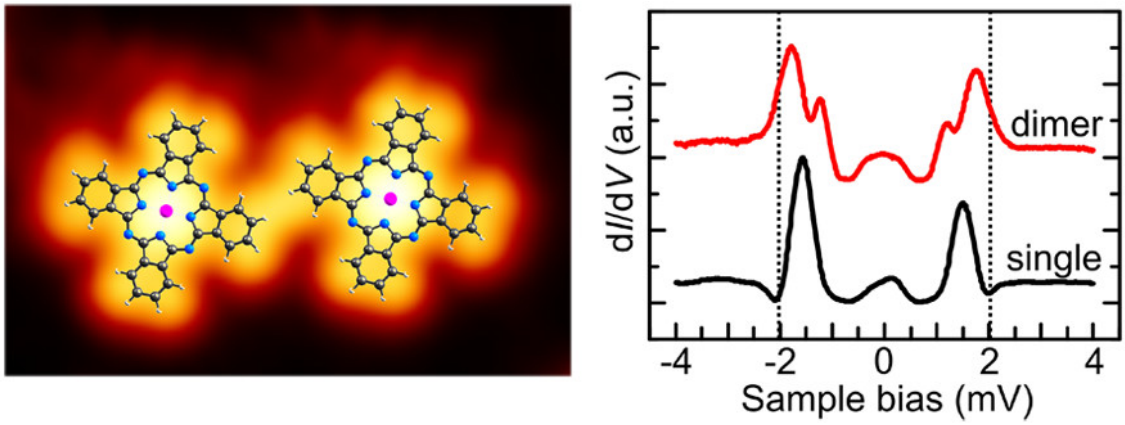

Figure 5: Topography scan image of coupled CoPC molecules and tunneling spectra of individual and coupled CoPc molecules. The spectra are measured on top of the magnetic cobalt atom in the center of the molecule with a superconducting STM tip. Image reproduced from [41].

It is also possible to couple several neighboring magnetic impurities to form so-called YSR bands. These hybridized YSR states have been shown to exhibit topological behaviour when arranged into specific lattice configurations [43, 44]. Various 2D geometries have been predicted to host topological phases [37], whereas certain 1D systems have even been realized experimentally [45].

2.2.5 Majorana zero mode (MZM)

In 1937 Ettore Majorana proposed a purely real solution to the Dirac equation, which results in a spin-1/2 fermionic particle that is identical to its own antiparticle [46]. These Majorana fermions have been researched vigorously in high-energy physics and astronomy, but so far Majorana fermions have not been definitively found in nature. Neutrinos have been suggested as examples of Majorana fermions [47], but definitive proof is still lacking [48].

Majorana fermions have also received wide interest in condensed matter physics. Theoretical studies of certain topologically non-trivial systems revealed creation and destruction operators that could produce Majorana-like quasiparticles. In particular, Moore and Read demonstrated a model Hamiltonian for so-called half-quantum vortices which involved Majorana quasiparticle wave functions and hosted non-Abelian exchange statistics [49]. Later the treatise was extended to generalized BCS theory by Ivanov, who showed that Majorana quasiparticles could emerge in vortices of a p-wave superconductor [13]. Kitaev then showed that such Majorana quasiparticles would localize to the ends of a 1D conductor with a single spin direction in proximity of a p-wave superconductor [50]. In Kitaev's theory, the Majorana quasiparticles emerge as zero-energy modes, which is why the quasiparticles are typically referred to as Majorana zero modes (MZMs). This also highlights the distinction to elementary Majorana fermions, which obey standard fermionic exchange statistics instead of non-Abelian ones.

A significant leap closer to experimentally available systems with MZMs was provided by Fu and Kane. They discussed a strong topological insulator with a proximity-induced gap from an s-wave superconductor, and showed that MZMs would be supported by vortices in such a system [51]. Removing the necessity of p-wave superconductivity greatly increases the number of potential materials capable of supporting topologically non-trivial states. Finally, Choy et. al proposed that a chain of magnetic nanoparticles on an s-wave superconductor would be sufficient to produce MZMs at the ends of the chain [52]. This result has been generalized for 2D magnetic lattices as well [53, 54].

It should be noted that observing edge states in magnetic islands on a superconducting surface is not necessarily evidence of MZMs [55]. There is no single "smoking gun" -experiment to distinguish MZMs from other quasiparticle excitations, but some expected properties of MZMs can be tested experimentally. For instance, the edge states corresponding to MZMs should exist at zero bias within the superconducting gap [4]. Secondly, the zero-bias conductance resulting from a MZM should be quantized in multiples of $e^2/\hbar$ [56]. Direct evidence for a MZM could be obtained with a direct measurement of the edge state exchange statistics, but a measurement setup required for this remains an unresolved issue.

A particularly hard experimental problem lies in the coupling between magnets and superconductors: if either one is strongly coupled to the other via covalent bonds, for instance, one of the opposing spin coupling types becomes dominant. This destroys either the magnetic or superconducting order, and thus no MZMs are observed. This limitation can be avoided by minimizing the coupling between the magnetic and superconducting layers of a system: the long-range orders of both can be maintained if other types of interactions are kept at a minimum. This can be achieved by using layered materials in which monolayers are bound to each other by weak vdW forces. These vdW -crystals include materials like graphene, and recently superconducting and ferromagnetic monolayer materials have been identified. These provide an ideal platform in the search of MZMs without unnecessary forms of coupling between the constituents.

2.3 Magnetism in 2D van der Waals crystals

After the peculiar electrical properties of graphene were discovered [57], a surge of research activity on 2D materials has emerged. Planar metals, semiconductors and superconductors were discovered in quick succession, and the effects of various perturbations such as strain and optical response have been investigated [58]. Among the latest developments is the discovery of materials that retain magnetic properties down to the monolayer limit, which we will discuss in this chapter. A brief introduction to models of 2D magnetism is followed by discussions of notable example materials: chromium triiodide (CrI_3) and magnetic transition metal dichalcogenides (TMDs).

2.3.1 Magnetic phenomena in 2D

Magnetism in two dimensions has been investigated theoretically for over a century, but only recent advances in surface science have made free-standing magnetic surfaces experimentally available in the monolayer limit. These systems make for ideal testing environments for old and new theoretical predictions on magnetism in 2D systems. Different forms of 2D magnetism with various coupling mechanisms and related phenomena are presented in figure 6.

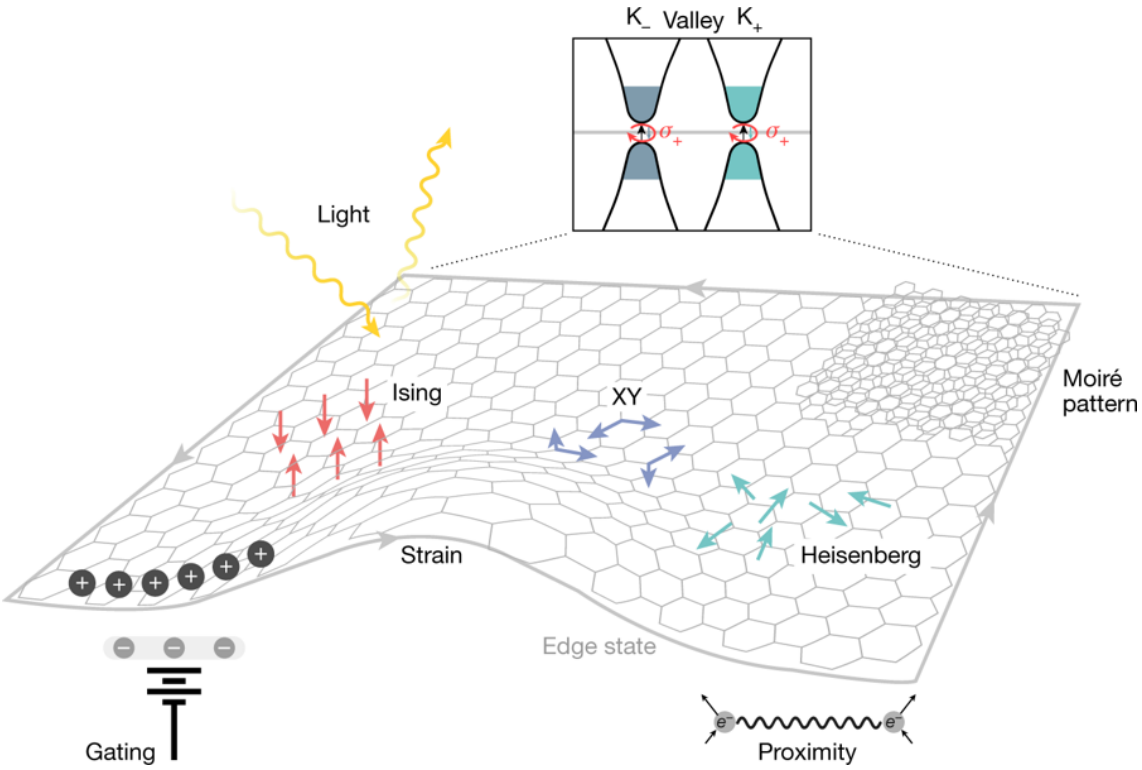

Figure 6: 2D magnetic vdW materials exhibit a rich tapestry of physics. The Ising, XY and Heisenberg models of 2D magnetism are highlighted by red, blue and green arrows, respectively. The magnetic ground states can be perturbed by strain, gating, proximity effects etc. Optical response, K-valley coupling and edge states can also provide insight into 2D magnetism. Image reproduced from [58].

The starting point for modelling 2D magnetism is determining the spin dimensionality of a particular system, or in other words the presence of easy and hard axes with respect to the lattice. In a system with a single preferred magnetisation axis, the possible spin values at a particular atom are binary, and thus the total magnetisation of the system is one-dimensional. Systems like these can be analyzed in the framework of the Ising model, which was analytically solved in 2D by Onsager [59]. The transition from an ordered to a disordered phase occurs through a second order phase transition at a critical temperature.

The spin vectors can also be confined to a particular plane, in which case the spin vectors are 2D at each lattice point. These systems are described by the XY-model, in which the spins are represented in terms of lattice vectors. The 2D XY-model does not exhibit a first- or second order phase transition at any finite temperatures [60]. However, correlations between spins decay differently over distance in the low- and high-temperature limits [1, 2]. This transition, discussed by Berezinskiĭ, Kosterlitz and Thouless, is the first example of a phase transition described in terms of topological order.

A further generalization of the XY model is the Heisenberg model, in which the spins have components in three dimensions. A 2D lattice with freely orienting spins does not transition into a long range ordered phase at any temperature [61]. If an easy axis or an easy plane exists in a 2D lattice, a generalized Heisenberg spin Hamiltonian is given by

$$\hat{H} = -\frac{1}{2}\sum_{i,j}\left(J\mathbf{S_i}\cdot\mathbf{S_j} + \Lambda S_i^z S_j^z\right) - \sum_i A\left(S_i^z\right)^2, \tag{23}$$

where J is the exchange coupling between neighbouring spins, Λ is the inter-site magnetic anisotropy, A is the on-site magnetic anisotropy and z denotes the spin component in the easy axis direction. The Ising- and XY models can be derived from this Hamiltonian by setting A to $\pm\infty$, respectively [61]. Tuning the coupling parameters results in a wide range of magnetic phenomena.

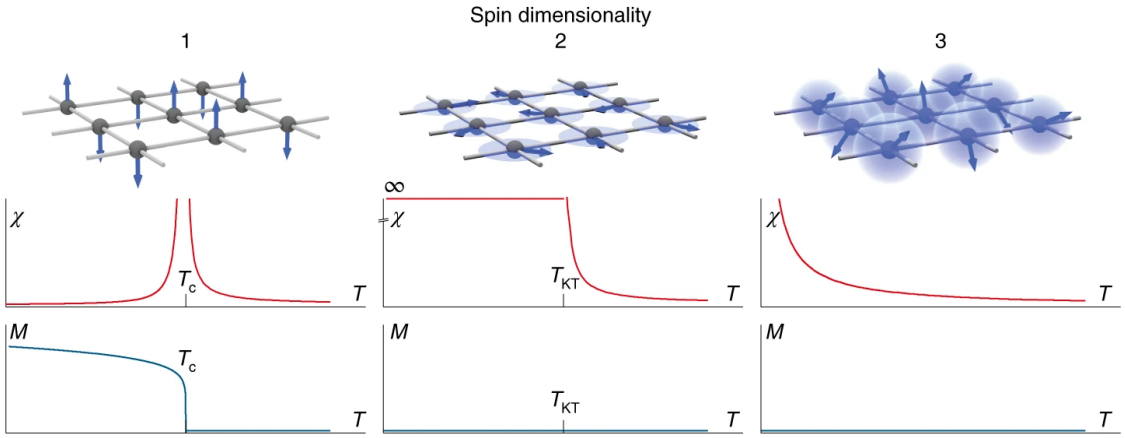

Figure 7: Magnetic susceptibilities (χ) and magnetisations (M) as functions of temperature for 2D lattices with Ising, XY and Heisenberg spin orientations. Image reproduced from [61].

Since the dimensionalities of both the lattice and spin orientations play a critical role in magnetic phenomena, the coupling between individual molecular layers must be minimized in order to experiment on 2D magnetism. The weakest form of interlayer bonding is mediated by vdW forces, which emerge due to temporary charge fluctuations between atoms and molecules. Crystals bound by vdW forces are easily exfoliated and cleaved due to the weak interlayer coupling, which makes them suitable for analysis with STM and other methods.

2.3.2 Ferromagnetic CrI_3

We shall now discuss the properties of some well-known vdW crystals with magnetic order. Chromium triiodide (CrI_3) is a notable example, being the first material in which 2D magnetism was observed in the monolayer limit [62]. The number of layers was shown to have a significant influence on the magnetic behaviour of CrI_3: a bilayer exhibits antiferromagnetic order as opposed to mono- and trilayers, which are ferromagnetic (see figure 8 for details). These changes in magnetic ordering are of particular interest in spintronics applications, where controlling the spin degree of freedom through electric fields has been a long-standing goal [63].

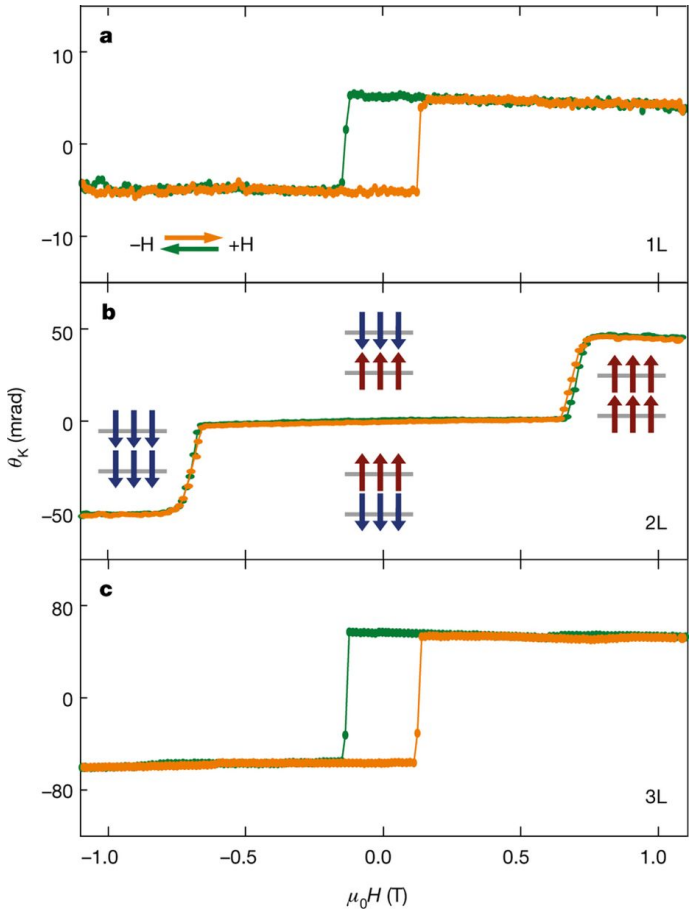

Figure 8: The magneto-optic Kerr effect (MOKE) in CrI_3 layers of varying thicknesses (1 to 3 monolayers in a, b and c, respectively). The Kerr angle θ refers to the phase difference between an incident and reflected laser beam, which depends on the magnetic order of the sample surface. The anisotropy associated with ferromagnetic order vanishes in the bilayer system. Image reproduced from [62].

In room temperature CrI_3 is a paramagnetic semiconductor [64]. The transition to a ferromagnetic (or antiferromagnetic) phase occurs at the Curie temperature 61 K for bulk and 45 K for monolayer samples. The layer structure also undergoes a transition from monoclinic to rhombohedral at a temperature range extending from 200 K to 150 K [64]. Figure 9 shows the rhombohedral structure and stacking of CrI_3.

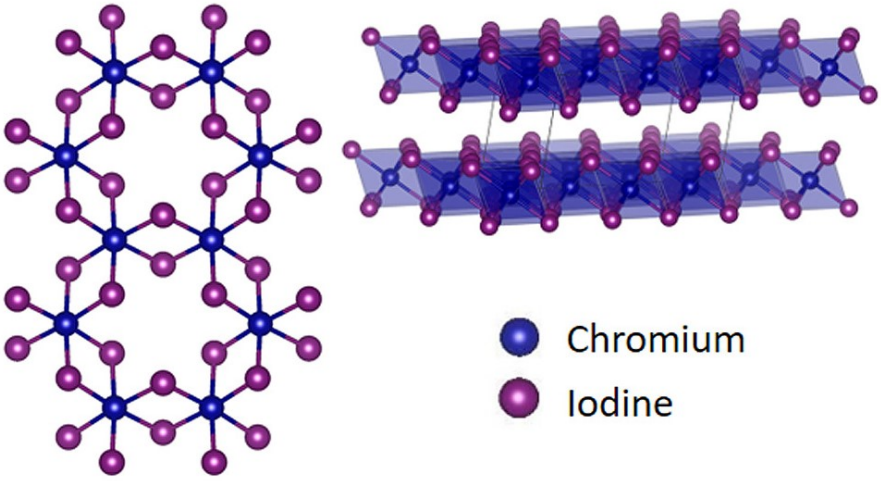

Figure 9: In-plane and out-of-plane structure of CrI_3 in low temperatures. In a rhombohedral structure the chromium atoms of consecutive layers overlap, which influences the average magnetization of the system. Image reproduced from [65].

Monolayer samples of CrI_3 have been produced by exfoliation from bulk crystals, since elemental iodine poses significant challenges for MBE and chemical vapor deposition (CVD) techniques. Bulk CrI_3 crystals can be synthesized from chromium powder and anhydrous iodine beads in sealed silica tubes where the center is kept at 650°C and the ends at 500 to 550°C [64]. Clean single crystals of CrI_3 degrade when subjected to moisture and light [65].

2.3.3 Magnetic transition metal dichalcogenides (TMDs)

TMDs are a class of materials with the structural formula MX_2, where M is a transition metal (V, Mn etc.) and X is a chalcogen (Se, Te etc.). TMDs form hexagonal lattices in monolayers bound to each other by vdW forces and have been shown to host a variety of long-range ordered phases. These include the superconducting niobium diselenide ($NbSe_2$) and magnetic materials such as vanadium diselenide (VSe_2) and manganese diselenide ($MnSe_2$).

TMDs typically exhibit one of three stable structural phases called trigonal prismatic (2H) and octahedral (1T, 1T') coordinations, see figure 10 for ball-and-stick visualizations. In the 2H phase the transition metal and chalcogen atoms are stacked in an ABA sequence with chalcogen atoms overlapping each other in the vertical direction, whereas in 1T and 1T' none of the atomic layers overlap.

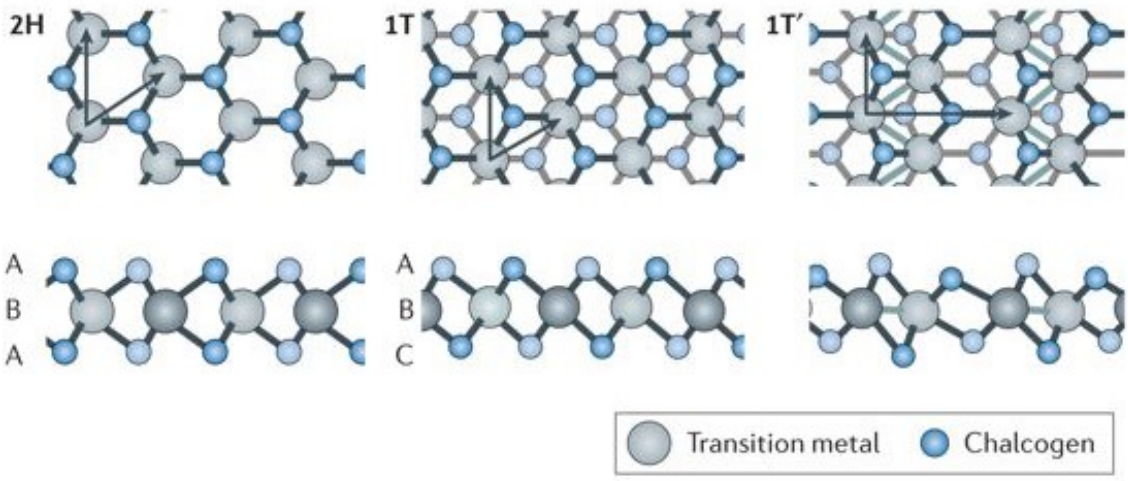

Figure 10: Ball-and-stick models of the structural phases of TMDs. Image reproduced from [66].

A key feature of TMDs is strong spin-orbit coupling: the individual spins of the lattice electrons interact strongly with their combined orbital angular momentum, resulting in otherwise degenerate states splitting in energy. This coupling can be exploited to create spintronic devices, where information can be encoded into the spin degree of freedom with electric fields only [63]. Spin-orbit coupling is influenced by IS breaking: bulk-induced asymmetry is called Dresselhaus coupling whereas interface- or surface-induced asymmetry is referred to as Rashba coupling. Strong spin-orbit coupling can also open finite band gaps, which can generate topological insulators of the $\mathbb{Z}_2$ type [66].

Several TMDs that retain magnetic properties in the monolayer limit have been identified through simulations [67] and experiments [5]. These include vanadium diselenide (VSe_2) and manganese diselenide ($MnSe_2$), both of which have a 1T-structure. Monolayers of VSe_2 and $MnSe_2$ can be mechanically exfoliated from bulk crystals or grown directly by MBE. Recent publications have caused dispute on whether pure VSe_2 monolayers remain intrinsically ferromagnetic: experiments by Bonilla et. al suggests that the monolayers remain ferromagnetic even in room temperature [5], whereas a computational study by Kim et al resulted in a Curie temperature of ~ 250 K [68]. Further ab initio calculations by Fumega and Pardo show that the ferromagnetic ground state is destabilized by the influence of charge density waves (CDW) [69], which has been confirmed experimentally by Coelho et al [70].

O'Hara et al found evidence of room-temperature magnetism in MBE-grown $MnSe_x$ thin films, and attributed the magnetic properties of the system to $MnSe_2$ monolayers [71]. The surface layers of their samples, however, consisted of bulk α-MnSe with a lattice constant of 3.9 Å, so their claim was not substantiated by direct STM measurements. Density functional theory (DFT) calculations by Kan et al estimate the lattice constant of 1T-$MnSe_2$ to be 3.6 Å [72], whereas a preceding DFT calculation by Ataca et al results in a lateral lattice constant of 3.27 Å [73].

Bulk $MnSe_2$ also exhibits a 3D cubic structure with a lattice constant of 6.4 Å [67]. Growth attempts of $MnSe_2$ could result in various phases of manganese selenide (MnSe), with a stable phase predicted to have a lattice constant of 4.2 Å [74] and unstable phases with lattice constants 3.6 Å and 3.85 Å [75, 76].

Since several phases of the grown compounds may coexist in the samples, conventional surface analysis techniques may not have sufficient spatial resolution to distinguish the electronic and magnetic properties of individual islands. An alternative to exhaustive growth parameter optimisation lies in atomic resolution measurement techniques, which will be discussed in the next section.

3 Experimental Methods

In this section we provide introductions to the essential measurement techniques and specific setups applied in the experiments. The quantum mechanical basis and practical operation of the STM is described, followed by a discussion on STS. The chapter concludes with a description of the MBE setup used in the experiments.

3.1 Scanning tunneling microscopy (STM)

Developed by Binnig and Rohrer in 1981 [77], the scanning tunneling microscope has enabled a host of experiments and advances in surface science. The device is operated by placing an atomically sharp tip close to a sample surface and measuring tunneling current at a given bias voltage and tip-sample distance. As opposed to the preceding surface measurement devices used to extract average quantities, STM allows for local measurements on the atomic scale. In addition to topographic imaging and spectroscopy measurements, STM setups are routinely used for atomic manipulation to form artificial nanostructures.

3.1.1 Principles of operation

To explain the electric current between an STM tip and a sample surface separated by a vacuum gap (in the absence of spark discharges), a classical model will not suffice: at small voltages the total energy of an electron in a solid is much smaller than the energy required to cross the vacuum gap. One must turn to quantum mechanics and the notion of non-local wave-functions to understand the behaviour of the system.

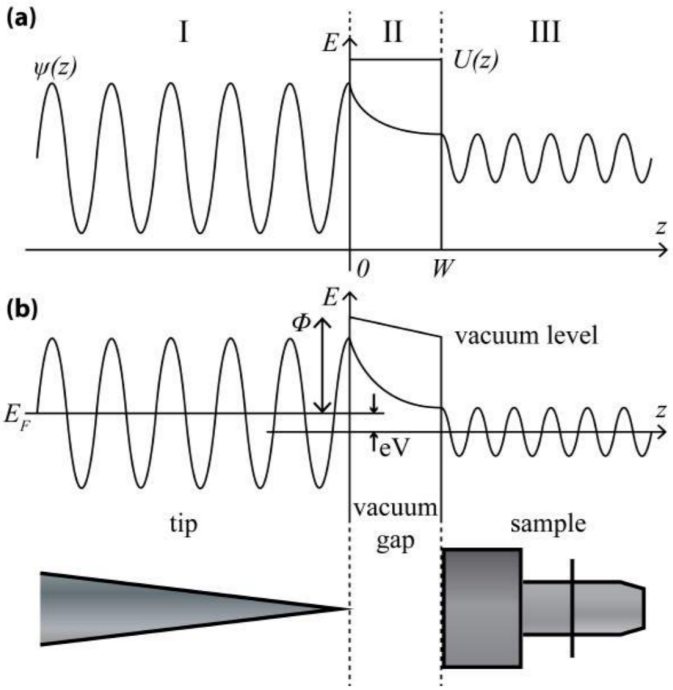

Figure 11: A tunneling junction at zero bias voltage (a) and a small applied bias voltage (b). The wave function in figure a) corresponds to an electron initially in area I (the tip). Image reproduced from [78].

Consider a one-dimensional system of two potential wells separated by an energy barrier of height ϕ and spatial width W as in figure 11. The Hamiltonian for a single electron in the system is given by

$$\hat{H} = T + V(z) = -\frac{\hbar^2}{2m}\frac{\partial^2}{\partial z^2} + V(z), \tag{24}$$

where

$$V(z) = \begin{cases} \phi, & 0 \leq z \leq W \\ 0 & \text{elsewhere.} \end{cases} \tag{25}$$

Under these conditions the time-independent solution for the Schrödinger equation $\hat{H}\psi(z) = E\psi(z)$ becomes a sinusoidal function on both sides of the potential barrier for $E > \phi$. At lower energies one also finds a solution within the barrier

$$\psi(z) = \psi(0)e^{-\kappa z}, \tag{26}$$

where the decay coefficient

$$\kappa = \frac{\sqrt{2m\,(\phi - E)}}{\hbar} \tag{27}$$

for a nearly constant $\phi(z)$. Thus the probability of observing an electron at a distance z in the barrier, given by $|\psi(z)|^2$, is proportional to $e^{-2\kappa z}$, which assumes non-zero values even for large barrier energies and distances in the z-direction.

A symmetric solution for inverted values of z also exists, which makes tunneling bidirectional. This symmetry can be broken by introducing a potential difference V across the barrier. Thus the total tunneling current observed will be proportional to the transmission coefficient

$$T := \frac{|\psi(z)|^2}{|\psi(0)|^2} = e^{-2\kappa z} = \exp\left(-2z\frac{\sqrt{2m\left(\phi - eV\right)}}{\hbar}\right). \tag{28}$$

In the context of STM, the potential barrier height ϕ corresponds to the work function of the surface material, i.e. the energy required to move an electron from Fermi energy to vacuum. At small bias voltages the transmission coefficient reduces to

$$T \approx \exp\left(-2z\frac{\sqrt{2m\phi}}{\hbar}\right). \tag{29}$$

With typical metals the work function is of the order 5 eV, which leads to a κ of $\sim$ 10 nm^{-1}. Thus an increase of 1 Å in tunneling distance z decreases the transmission coefficient, and consequently the tunneling current, by an order of magnitude. This exponential dependence on tunneling barrier width results in the extreme current sensitivity of an STM tip, allowing for topography measurements at atomic resolution. Figure 12 shows a simplified schematic of an STM measurement setup.

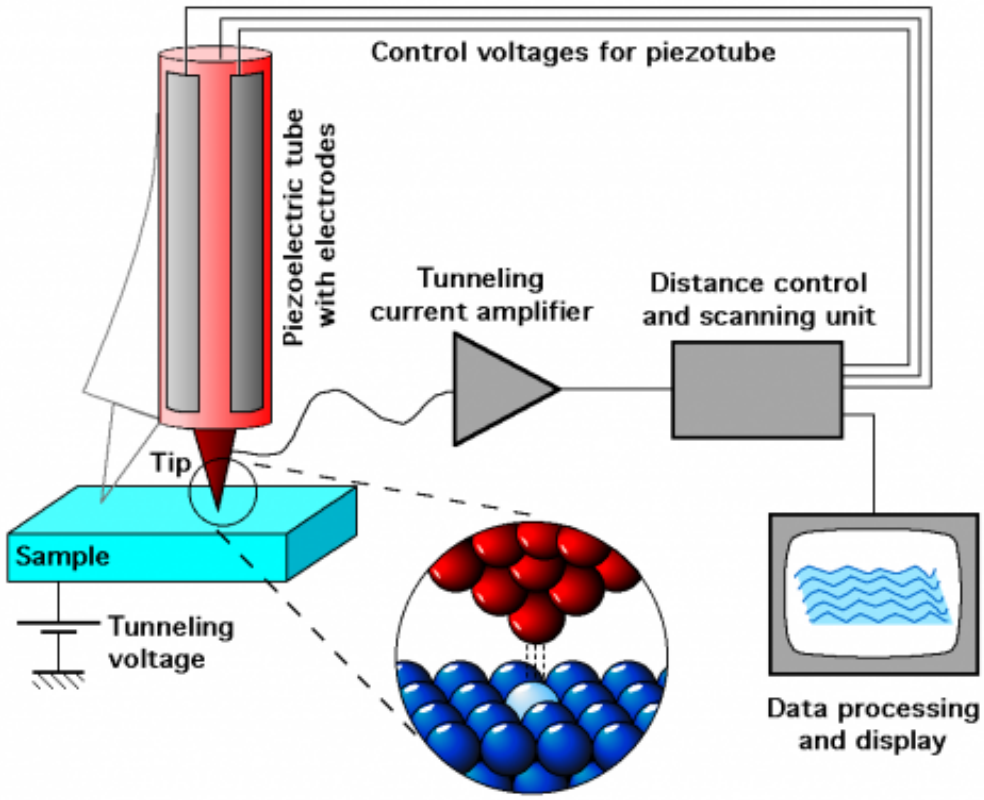

Figure 12: A simplified schematic of an STM setup. The tunneling current typically ranges from 10 pA to $\sim 1-2$ nA, so high-quality electronics are needed to keep the noise levels sufficiently low. Image reproduced from [79].

The primary adjustable variables in an STM measurement are tip position and bias voltage between the tip and the sample. A specific tunneling current can be obtained by adjusting the tip height at a certain bias voltage. By controlling the tip height in a feedback loop, a specified tunneling current can be maintained while keeping the bias voltage constant. By scanning the surface with the tip while using the height control feedback one obtains a constant current map, where the height signal corresponds to differences in the local density of electron states (LDOS) close to the Fermi level. With sufficiently high current setpoints ($\sim$ 1 nA) and low bias voltages ($\sim$ 100 mV) an atomic resolution height contour emerges. This operation mode is referred to as constant current mode.

To probe the LDOS at a certain bias and height, one can also measure the current signal directly without applying a height control feedback. This operation mode is called constant height mode and is used to probe the local electronic structure of a sample surface at specific energies. Constant height maps can be used to investigate the molecular orbitals of a sample molecule or surface, since different orbitals contribute to the tunneling current at different energies.

3.2 Scanning tunneling spectroscopy (STS)

The tunneling current over a junction depends on the availability and occupation probabilities of different electronic states. Thus measuring tunneling current through an STM tip at varying bias voltages provides information about the local electronic structure of a sample. This method, referred to as scanning tunneling spectroscopy (STS), has been utilized in various surface-adsorbate systems, such as magnetic molecules on superconducting surfaces [41]. STS can also be used to characterize the structure of an STM tip apex, which is a variable of paramount importance for performing reproducible measurements.

STS is performed by fixing the STM tip at a specific height above a surface or adsorbate of interest. Instead of determining an absolute height between the tip apex and the feature, the height can be adjusted by employing a feedback loop to set the height according to a specific tunneling current setpoint at a chosen bias voltage. When the tip position is fixed, the tunneling current is measured as a function of bias voltage over a specified range. The process can be repeated at any number of points to see changes in tunneling conductivity over a specified line segment or surface.

A variable of particular interest in STS measurements is the differential conductance (dI/dV) of a sample, since this can be directly related to the LDOS as shown in the following subsection. A direct numerical differentiation of the tunneling current typically leads to low signal-to-noise ratios, so in practice the dI/dV is measured directly using lock-in amplifiers and a sinusoidal voltage modulation. When the bias voltage is modulated sinusoidally with constant amplitude and frequency, the corresponding tunneling current amplitude at the modulation frequency is directly proportional to the dI/dV [80] (see figure 13 for a visualisation of this principle). A lock-in amplifier removes all other frequency components from the current signal, resulting in decreased noise contribution to the dI/dV-spectra. The energy resolution of a spectroscopy measurement is determined by the voltage modulation amplitude, the noise level at the chosen modulation frequency and various experimental factors such as electron temperature and tip DOS.

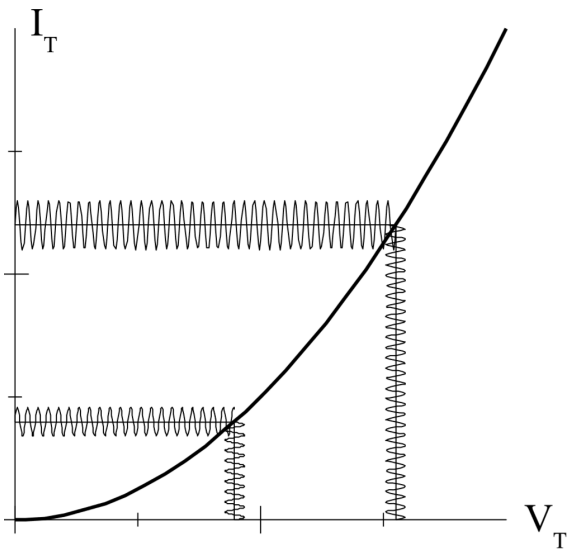

Figure 13: When the bias voltage V_T is sinusoidally modulated, the resulting tunneling current amplitude I_T is proportional to $\frac{dI}{dV}\Big|_{V=V_T}$. The voltage resolution of the dI/dV is limited by the voltage modulation amplitude. Image reproduced from [80].

3.2.1 Relation between dI/dV and LDOS

The density of states of a material is defined as the number of available states per unit volume within a narrow energy window $E + dE$. At atomic length scales the density of electron states has a spatial dependence on the atom positions, which is why STM literature typically makes the distinction between a local density of states on a surface (LDOS) and a bulk density of states (DOS). The LDOS is defined as

$$\rho(\mathbf{r}, E) = \sum_{\nu} |\psi_\nu(\mathbf{r})|^2 \delta\left(E - E_\nu\right), \tag{30}$$

where $\delta(E)$ is the Dirac delta. The tunneling current from an STM tip to sample depends on the tip DOS $\rho_t(E)$, the sample LDOS $\rho_s(E)$, the occupation probabilities of the states (given by the Fermi-Dirac distribution) and finally the wave function overlap between the tip and the sample. Figure 14 illustrates the LDOSes and Fermi-Dirac distributions in a metallic tunneling junction. By applying the tunneling Hamiltonian formalism developed by Bardeen [81], the tunneling current from tip to sample becomes

$$I_{t\to s} = \frac{4\pi e}{\hbar} \int_{-\infty}^{\infty} \rho_t(E - eV)\rho_s(E) f(E - eV)\left(1 - f(E)\right) |M(E - eV, E)|^2 dE, \tag{31}$$

where V is the applied bias voltage, $E = 0$ corresponds to the Fermi energy of the sample and

$$f(E) = \frac{1}{1 + e^{\frac{E}{k_B T}}} \tag{32}$$

is the Fermi-Dirac distribution. The tunneling matrix element term describing the overlap of wave functions at specific energies can be written in one dimension as

$$|M(E-eV,E)|^2 = \exp\left(-2z\sqrt{\frac{m_e}{\hbar^2}\left(\Phi_t+\Phi_s-eV+2E\right)}\right), \tag{33}$$

where z is the tip height and Φ_t and Φ_s are the work functions of the tip and the sample, respectively. Another approximate expression of M was derived by Tersoff and Hamann by assuming a constant tip DOS and a point-like tip apex [82].

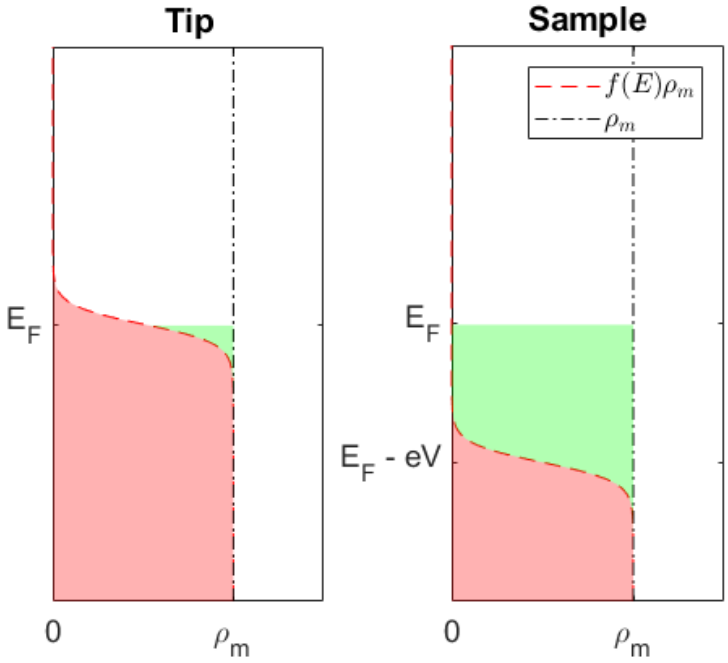

Figure 14: A metallic tunnel junction at 4 K. The LDOS of metals can be assumed constant close to the Fermi level. The vacancies generated by thermal excitations and bias voltage are highlighted with green, whereas occupied electron states are highlighted with red.

To derive the total observed tunneling current, the tunneling events from sample to tip must also be accounted for due to the thermal broadening of the Fermi-Dirac distributions (even when the sample is at lower bias, there are bound to be some electrons at sufficiently high energy states to tunnel into the tip). The total tunneling current thus becomes

$$I = I_{t\to s} - I_{s\to t} = \frac{4\pi e}{\hbar}\int_{-\infty}^{\infty}\rho_t(E-eV)\rho_s(E)\left(f(E-eV)-f(E)\right)|M(E-eV,E)|^2 dE. \tag{34}$$

A series of approximations can be applied to equation 34 to interpret the relation between dI/dV spectra and the sample LDOS. Firstly, the tunneling matrix element can be considered constant in the low bias limit ($eV << \Phi_t + \Phi_s$). With this assumption the bias derivative of equation 34 becomes

$$\frac{\partial I}{\partial V} \propto \int_{-\infty}^{\infty} \rho_s(E) \, (\, -\rho_t'(E-eV) f(E-eV) \\ - \rho_t(E-eV) f'(E-eV) \\ + \rho_t'(E-eV) f(E) \,) \, dE, \tag{35}$$

where $\rho_t' = \frac{\partial \rho_t}{\partial V}$ and

$$f'(E) = \frac{\partial f(E)}{\partial V} = -\frac{1}{2k_B T} \mathrm{sech}^2 \left(\frac{E}{k_B T} \right) \xrightarrow{T \to 0} -\delta(E). \tag{36}$$

By assuming a constant tip DOS, the low temperature limit of equation 35 becomes

$$\frac{\partial I}{\partial V} \propto \rho_t \int_{-\infty}^{\infty} \rho_s(E) \delta(E-eV) dE = \rho_t \rho_s(E-eV). \tag{37}$$

To summarize, dI/dV is proportional to the sample LDOS at low temperatures and small bias voltages when the tip DOS is constant. The final assumption is typically the hardest to confirm experimentally since the atomic configuration of the STM tip apex is prone to change due to voltage changes, interactions with the sample surface etc.

It should be noted that an optimal tip DOS for spectroscopy is not necessarily optimal for topography measurements: a Dirac delta -like DOS around Fermi energy would result in perfect energy resolution, whereas with a constant DOS the energy resolution is always limited by the broadening of the Fermi-Dirac distribution [80]. Practical analogues of these extremes are superconducting and metallic STM tips, respectively. Superconducting tips provide increased energy resolution due to the sharp increase in tip DOS at the edges of the superconducting gap, although the measured spectra must be deconvolved to obtain the surface LDOS.

3.3 Molecular beam epitaxy (MBE) setup

Molecular beam epitaxy is a synthesis process in which beams of evaporated atoms or molecules are directed on a sample substrate, where they self-assemble to form various structures [83]. MBE is routinely used to synthesize compounds and heterostructures with atomic precision, although the necessity of ultra-high vacuum (UHV) conditions makes the technique slightly less accessible than chemical vapour deposition (CVD), for instance.

Different materials require different types of evaporators: selenium, for instance, can be evaporated in a Knudsen-type thermal effusion cell, whereas metals with high melting points require electron beam evaporators. The Knudsen cell evaporator consists of a crucible which is heated by a filament to produce a flux of evaporated atoms or molecules. The evaporated materials may form clusters of various sizes, which can be broken down further with a cracker cell.

The electron beam evaporator is used to evaporate materials with high melting points. Typically the evaporant is a solid rod which is bombarded by an electron

beam generated by a high voltage filament. When the energy of the electron beam is sufficiently high, atoms start evaporating from the rod. The electron beam generates substantial heating power, so water cooling is typically required for stable operation.

The MBE setup used in the experiments involved a Createc OLED Knudsen cell evaporator for selenium and a Focus EFM 3 e-beam evaporator for manganese. The flux of evaporated selenium was monitored indirectly through the cell temperature and preparation chamber pressure, whereas the manganese flux was monitored with a flux monitor built into the e-beam evaporator. Previous syntheses of $MnSe_2$ [71] have not shown significant sensitivity to the selenium flux, and thus more accurate flux measurements were not deemed necessary.

The substrate temperature is a critical variable dictating the possible reactions routes and reaction thresholds on the surface. The substrate was heated with direct current heating through the sample holder and also by electron beam heating. The heating power of the latter method is very sensitive to the acceleration bias of the electron beam, which was used to fine-tune and stabilize the temperature. A SensorTherm Metis MP25 pyrometer was used to measure the substrate temperature, since a thermocouple connection was not available in the system.

4 Results and discussion

In this section we present and discuss the results of topography and spectroscopy. The measurements were performed in a Unisoku USM-1300 low temperature STM with a gold-coated platinum-iridium tip. Gwyddion and WSXM software were used to analyze and process the topography data [84, 85], whereas spectroscopic data was analysed with SpectraFox [86] and Matlab.

A short description of the failed growth experiments on highly oriented pyrolytic graphite (HOPG) is followed by topography measurements on successfully grown $MnSe_x$ islands on a $NbSe_2$ substrate. The growth parameters of certain exemplary samples are also presented. The topography results are followed by spectroscopic measurements on the various samples. The topography scan images are corrected by linear background removal unless otherwise stated.

4.1 Sample growth and characterization by STM

4.1.1 Growth on HOPG substrate

To optimize the growth parameters of $MnSe_2$ in a cost-efficient manner, the initial growth experiments were performed on a HOPG substrate instead of the superconducting $NbSe_2$. Both substrate materials are vdW-crystals with a hexagonal lattice structure and these commonalities were expected to result in similar growth conditions for $MnSe_2$. This assumption was supported by previous experiments with vanadium diselenide (VSe_2), where epitaxial growth was achieved in roughly the same conditions for both substrates [87].

The initial growth parameters were chosen based on the VSe_2 experiments due to the structural similarity of VSe_2 and $MnSe_2$. The primary growth variables were

- Sample temperature
- Deposition time
- Manganese flux
- Pressure increase due to selenium evaporation
- Annealing temperature
- Annealing time.

A number of depositions were made in various growth conditions and the resulting samples were analyzed at 77 K. No $MnSe_2$ islands were found despite extensive variations in sample temperature (20 °C to 300 °C) and manganese flux. The most notable surface features were identified as amorphous manganese clusters: selenium was expected to desorb quickly due to its high partial pressure. Figure 15 shows a large area scan and an atomic resolution image after a growth attempt. Samples with only manganese evaporated on them were mostly indistinguishable from samples subjected to both manganese and selenium.

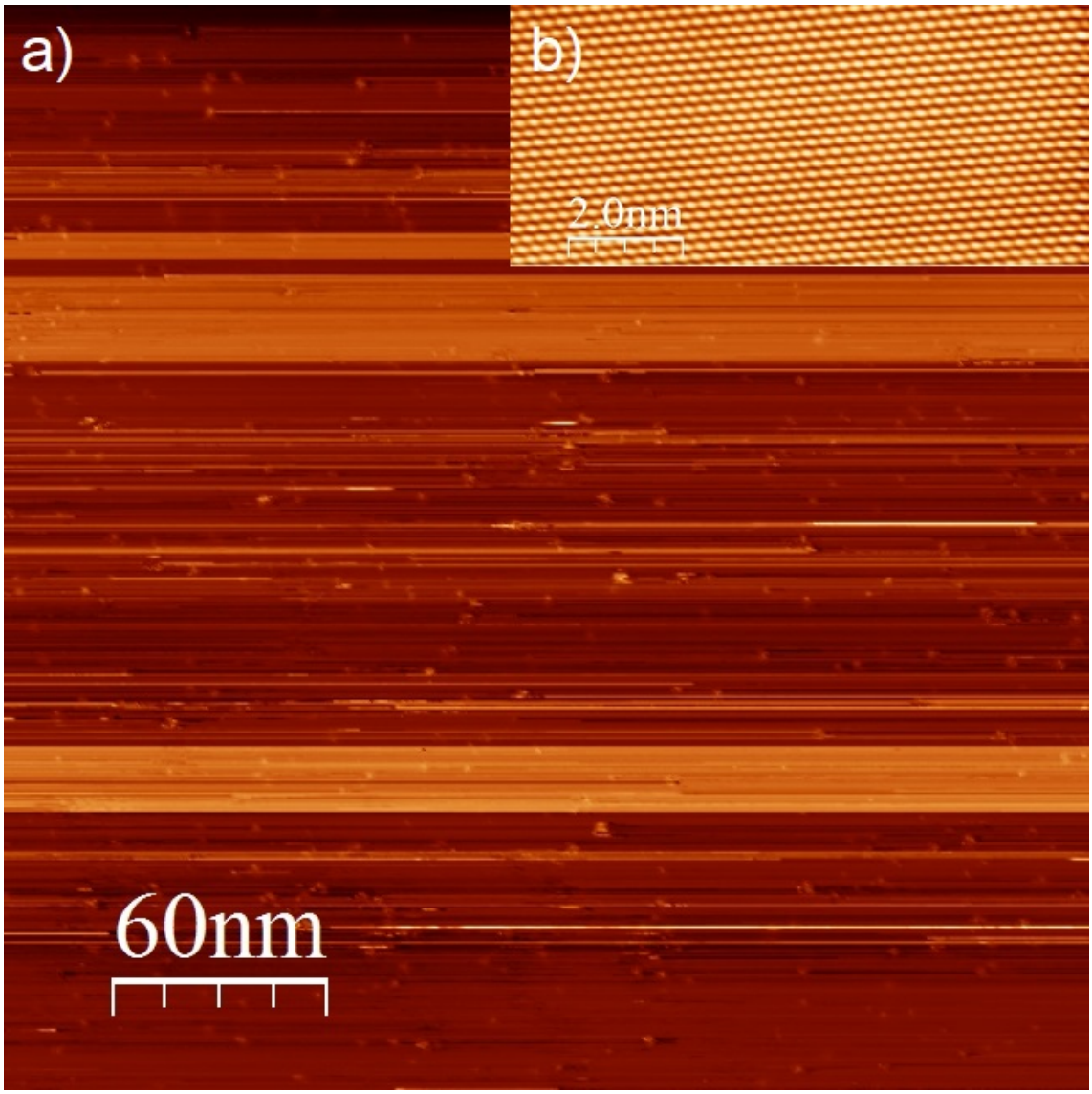

Figure 15: **a)** A large scale scan showing only mobile manganese clusters after deposition. Bias 1 V, current 50 pA. **b)** Atomic resolution image of the substrate showing a lattice constant of 2.431 Å, consistent with graphite. Bias 100 mV, current 1.5 nA. Scans performed at 77 K.

Definitive reasons behind the failed synthesis of $MnSe_2$ were not identified, but various explanations can be postulated. A heuristic used in other MBE syntheses suggests that materials with high lattice mismatches refuse to form stable islands epitaxially due to various strain effects [83]. The mismatch for $MnSe_2$ and HOPG is approximately 50%, whereas for VSe_2 the mismatch is slightly smaller ($\sim 40\%$). The fact that interlayer coupling between vdW-crystals should be negligible contradicts this explanation, although it is possible that the vdW monolayers form around more tightly bound nucleation centers. Another possibility is that substantial amounts of manganese intercalates into the HOPG via step edges and lattice defects, hindering island growth. Intercalation probability is temperature dependent [88], and for

HOPG the onset temperature of significant intercalation might be lower than the temperature required for $MnSe_2$ island formation. Further experiments on HOPG were not deemed necessary, since HOPG was only meant to serve as a test platform for growth on $NbSe_2$.

4.1.2 Growth on $NbSe_2$ substrate

After the growth experiments on HOPG, the substrate was switched to the superconducting $NbSe_2$. The bulk crystal was attached to the sample holder with a two-part silver epoxy adhesive and cleaved in high vacuum ($\sim 2 \cdot 10^{-7}$ mbar) with Scotch tape. The growth process was kept the same as with HOPG: the sample was heated to a desired temperature, after which Mn and Se were codeposited on the sample. After the deposition the sample was annealed while there was still excess selenium in the preparation chamber. Table 2 summarizes the growth parameters of the successfully synthesised samples: the following sections will apply the same notation to refer to individual samples.

Table 2: Growth parameters of samples with successfully deposited $MnSe_x$ islands, where T_s is the substrate temperature, t_d is the deposition time, I_{Mn} is the Mn flux, p_d is the deposition pressure, T_a is the annealing temperature and t_a is the annealing time.

Sample	T_s (°C)	t_d (min)	I_{Mn} (nA)	p_d (mbar)	T_a (°C)	t_a (min)
A	240	5	5	$1.0 \cdot 10^{-8}$	230	5
B	240	5	5.5	$1.4 \cdot 10^{-8}$	240	12
C	215	10	10	$1.0 \cdot 10^{-8}$	225	10
D	215	5	10	$3.0 \cdot 10^{-8}$	220	21
E	215	5	5	$2.0 \cdot 10^{-8}$	215	16

The initial growth parameters used on HOPG were kept constant for the first growth attempt on $NbSe_2$, which immediately produced islands with diameters over ~ 20 nm as shown in figure 16. Large scale and atomic resolution STM images were taken in 77 K. The measured lattice constants for the substrate and the islands were 3.3 Å and 4.25 Å respectively, corresponding to 2H-$NbSe_2$ and bulk MnSe [74].

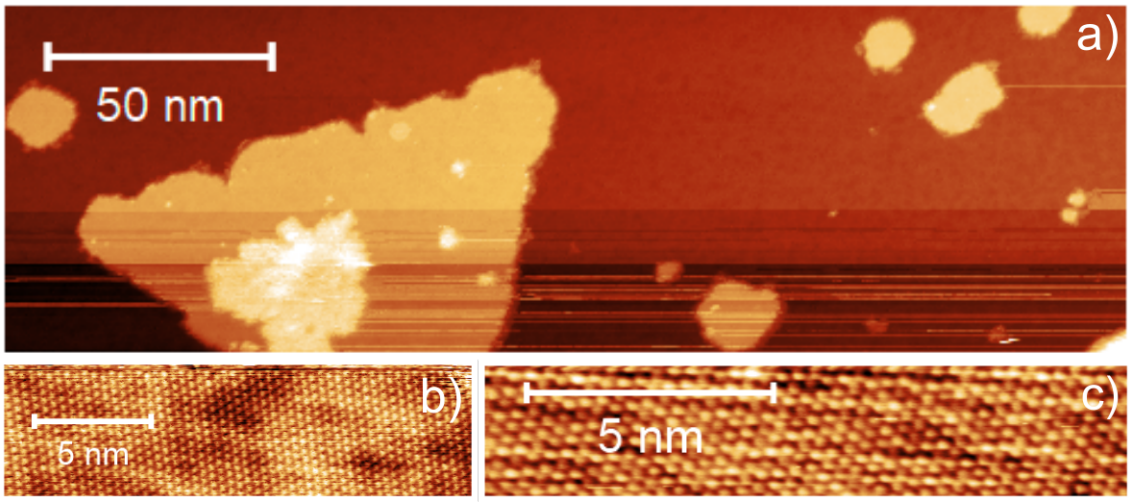

Figure 16: **a)** A large scale scan of sample A showing large islands with aligned edges. Bias 1.8 V, current 10 pA. **b)** Atomic resolution image on the island with a lattice constant of 4.25 Å, consistent with bulk MnSe. Bias 1.8 V, current 1 nA. **c)** Atomic resolution image of the substrate with a lattice constant matching $NbSe_2$ ($\sim$ 3.3 Å). Bias 157.5 mV, current 1 nA. Scans performed at 77 K.

After the initial growth attempt the microscope was cooled down to 4 K to see whether the $NbSe_2$ would retain its superconductivity in the presence of the islands. For this purpose, sample B was prepared with the same growth parameters as sample A. The characteristic CDWs of $NbSe_2$ were not found in the atomic resolution images. As shown in figure 17, the substrate exhibited significant disordered contrast changes at atomic resolution, suggesting manganese intercalation into the substrate [89]. To prevent this in subsequent samples, the growth temperature was lowered from 240 °C to $\sim$ 215 °C. Figure 18 shows the large area structure and atomic resolution images on the islands and the substrate. The islands on sample B had a lattice constant of 3.56 Å, corresponding to $MnSe_2$ or an unstable phase of MnSe [75].

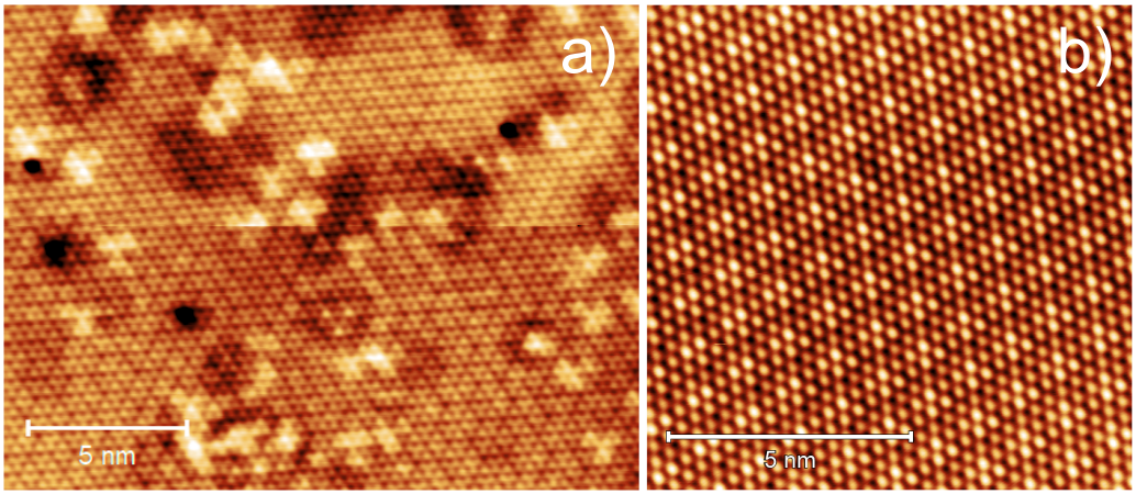

Figure 17: **a)** Atomic resolution image of the $NbSe_2$ surface of sample B. Bias -50 mV, current 300 pA. **b)** A pristine $NbSe_2$ surface, bias 20 mV, current 1 nA. The CDW is absent in image a), suggesting Mn intercalation into the $NbSe_2$ layers. Both scans performed at 4 K temperature.

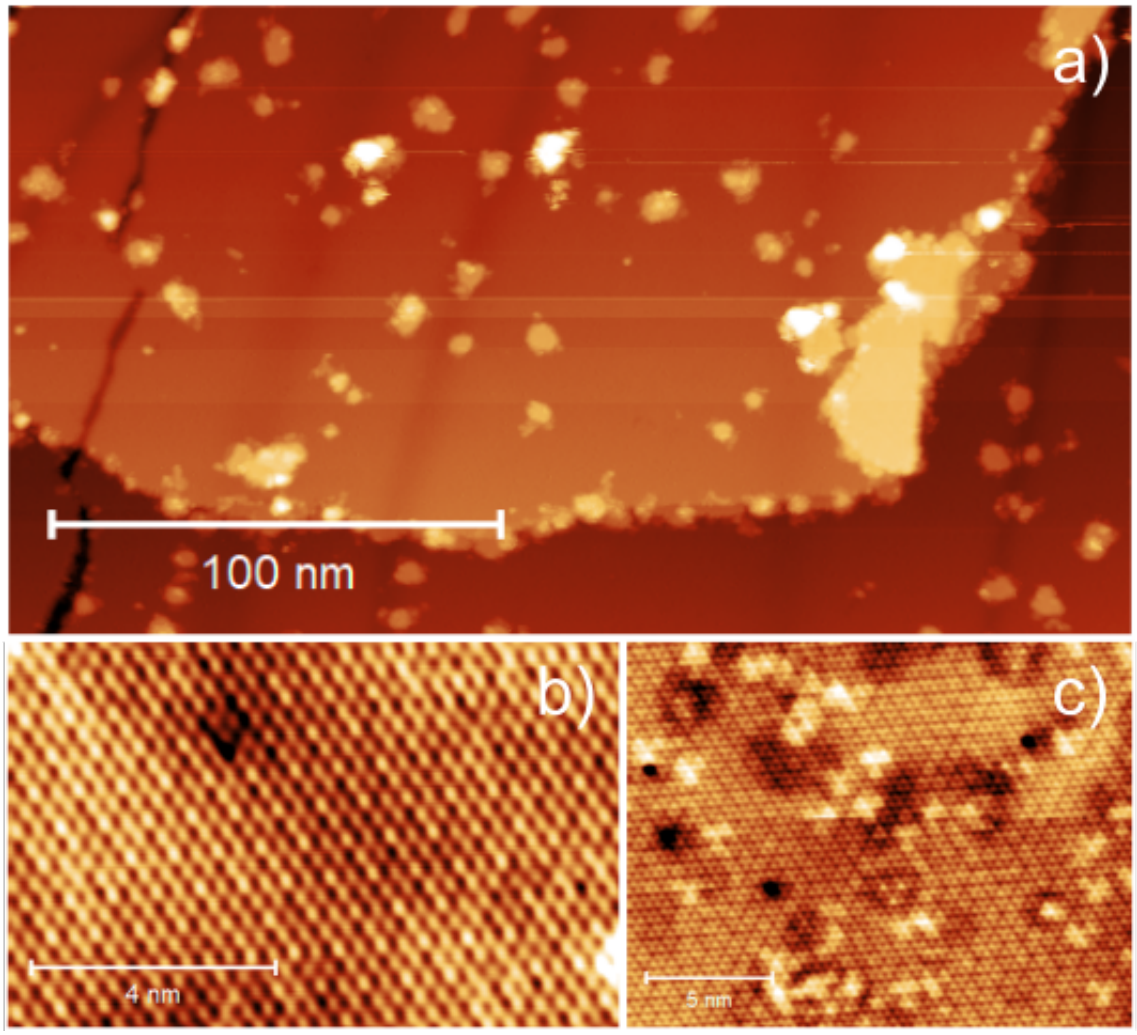

Figure 18: **a)** Large area scan of sample B with multiple layers of $MnSe_x$. Bias 1 V, current 10 pA. **b)** Atomic resolution scan of the top layer, lattice constant 3.6 Å. Bias 100 mV, current 1 nA. **c)** Atomic resolution on the bottom layer, lattice constant 3.4 Å. Bias −50 mV, current 1 nA. Scans performed at 4 K.

After adjustments to the experimental setup and a few iterations of depositions with different growth parameters, samples with atomically sharp island edges were obtained. Most of the sharp edges were similarly aligned with respect to the substrate, but whether the edge terminations were atomically identical was not definitively confirmed. In sample C the island coverage exceeded one monolayer and the $NbSe_2$ surface could not be identified. Large scale and atomic resolution images of this sample are presented in figure 19. The first and second layers of $MnSe_x$ islands showed different lattice constants. The larger measured lattice constants (4.3 Å and 3.8 Å) are consistent with bulk MnSe formation, whereas the 3.56 Å phase is either $MnSe_2$ or an unstable phase of MnSe. In some scans the lattice constants were not uniform in all directions, suggesting drift issues, noise or too high scanning speeds. The 3.8 Å phase, corresponding to $\alpha-$MnSe [71], could not be reproduced in

subsequent samples. No significant differences in island heights were observed in the samples, suggesting similar stacking between the atomic layers of the compounds. Histograms of measured lattice constants and island heights are given in appendix B.

Spectroscopy on the islands showed the superconducting energy gap of $NbSe_2$ due to the proximity effect. Interestingly the gap was more prominent on the second layer of islands, suggesting a decreased net magnetisation due to the magnetic coupling between layers (see figure 21 for details).

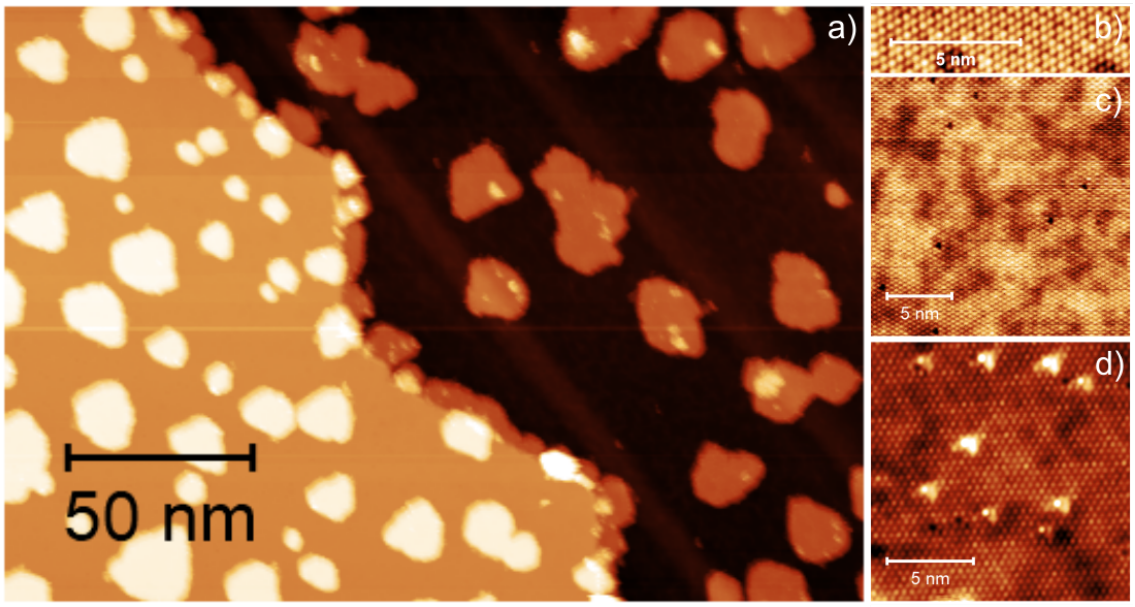

Figure 19: **a)** Large area scan of sample C with multiple layers of $MnSe_2$ and different lattice constants. Bias 1 V, current 20 pA. **b)** Bottom layer, lattice constant 3.56 Å. Bias −551.2 mV, current 1 nA. **c)** First island layer, lattice constant 3.8 Å. Bias 100 mV, current 1 nA. **d)** Second island layer, lattice constant 4.3 Å. Bias 500 mV, current 500 pA. Scans a) to c) performed at 4 K, whereas d) was performed at 300 mK.

Finally samples with sub-monolayer coverage and aligned islands were synthesized. Samples D and E had large islands up to $\sim$ 100 nm in diameter with trace amounts of (presumably) selenium adatoms on the $NbSe_2$ surface and the islands. Atomic resolution images at 300 mK, such as the ones presented in figure 20, show a moiré pattern which coincides with the preferred adsorption sites of the adatoms. The relative angle between the $NbSe_2$ and MnSe lattices was estimated to be 0.797° with a lattice mismatch of 29.17%. The moiré pattern had a wavelength of 18.1 Å at a 2.73° angle with respect to the $NbSe_2$ lattice shown in figure 20 b. [90]. The Fourier filtered components of figure 20 c) corresponding to the island lattice and the moiré pattern are given in appendix A.

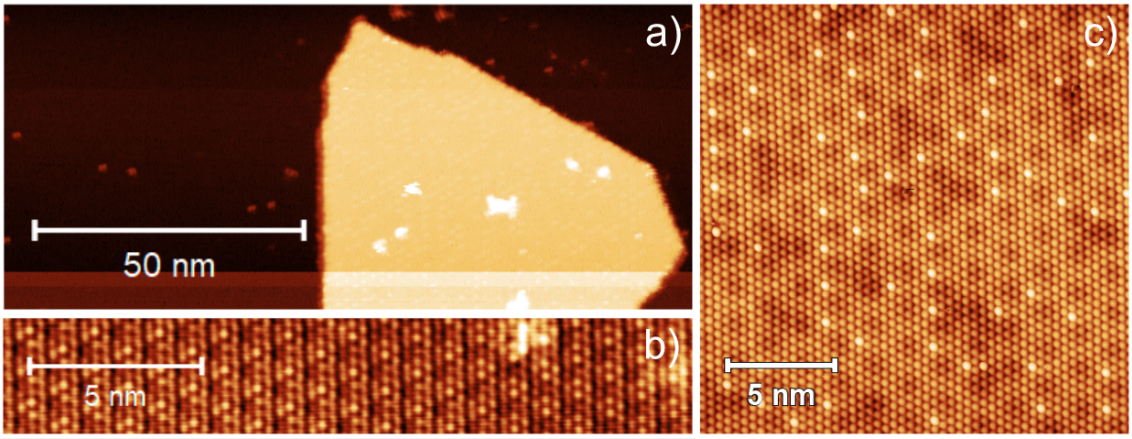

Figure 20: **a)** Large area scan of an island on sample E. Bias 1 V, current 10 pA. **b)** Atomic resolution image of the substrate, lattice constant 3.497 Å. Bias −78.74 mV, current 500 pA. **c)** Atomic resolution image on the island showing a moiré pattern and impurity atoms with preferred adsorption sites. Lattice constant 4.571 Å, bias −157.5 mV, current 500 pA. All scans performed at 300 mK.

4.2 STS measurements

STS was performed on successfully synthesized samples in 4 K and 300 mK temperatures. Although multiple samples with atomically sharp $MnSe_x$ island edges were synthesized, no evidence of edge states was found through spectroscopy. The most prominent signs of magnetic order were observed in the high coverage sample C shown in figure 19, where the superconducting gap magnitude increased on the second layer island. This could be interpreted as the same kind of layer-dependent magnetic order as observed in CrI_3, but the effect could not be replicated in the following samples. This was also the only sample with a 3.8 Å phase, suggesting that this particular phase could support magnetism in the monolayer limit. The absence of edge states contradicts this interpretation, although it is not clear whether this phase formed as a vdW layer. Line spectroscopy and averaged spectra on the top layer islands are presented in figure 21.

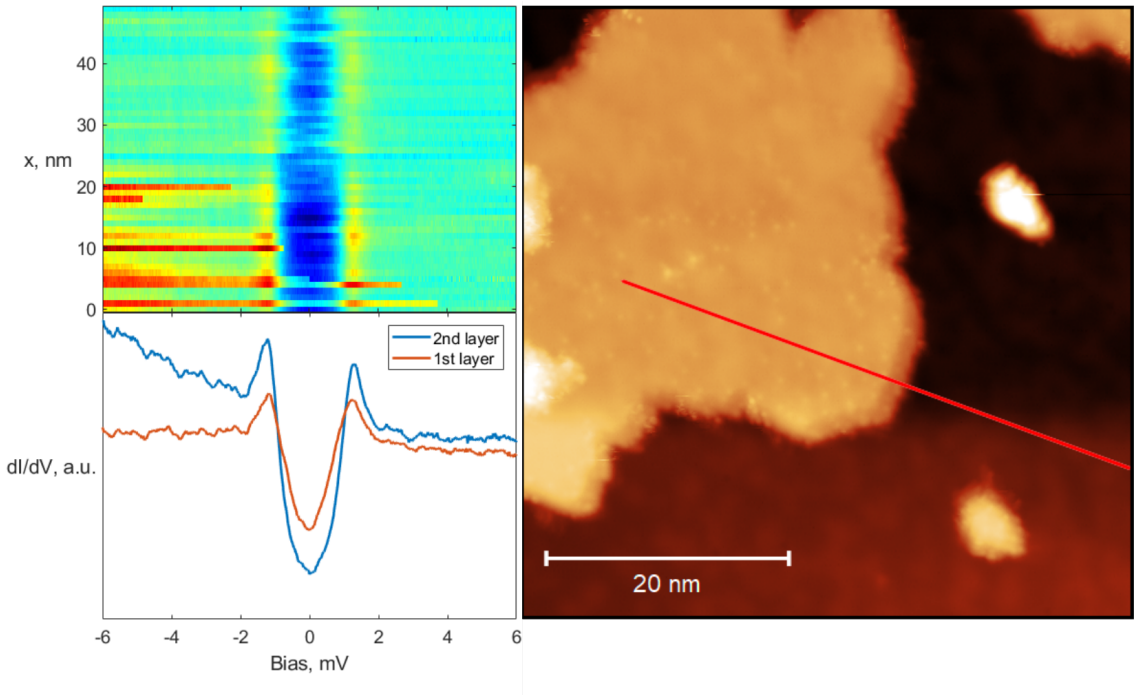

Figure 21: Line spectra on the highest island layers of sample C exhibit a change in the superconducting gap. Voltage modulation 0.2 mV in the spectra, scan bias 800 mV, current 800 pA. The line trajectory (length 50 nm) is centered on the island edge with the point $x = 0$ nm on the second layer. The average spectrum on the second layer is distorted by tip events in the negative bias range. Topography and spectra measured at 300 mK.

Figure 22 shows dI/dV maps of islands with a lattice constant of 4.3 Å on sample D. Although individual points with higher zero bias conductance are visible on some of the island corners, the conduction difference with respect to the background is minimal and no continuous zero bias conductance channels were found. The island edges are indistinguishable in dI/dV maps at bias voltages smaller than the superconducting gap.

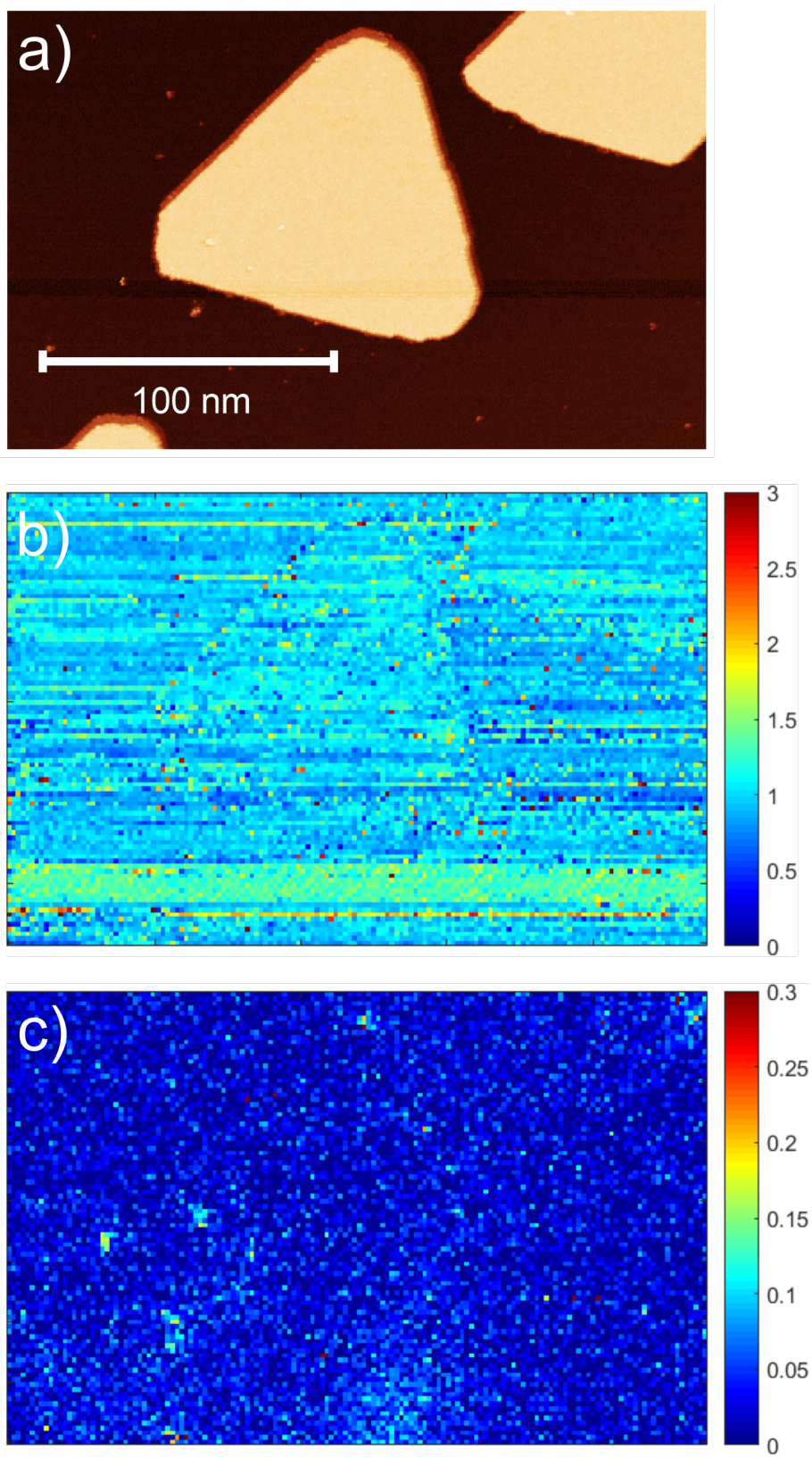

Figure 22: **a)** Plane corrected large scale image of MnSe islands on sample D. Bias -1 V, current 5 pA. **b)** -3 mV conductance map of the same area as a) with visible island edges. Modulation voltage 0.2 mV. **c)** Zero bias conductance map of the same area. The island edges exhibit only faint conductance peaks at individual points. Scan and spectra measured at 300 mK temperature.

Figure 23 shows a line spectroscopy scan crossing an island layer on sample D. The superconducting gap of $NbSe_2$ permeated onto the island layers and remained almost constant throughout the line, indicating that no magnetic moment or other impurities were interfering with the order parameter magnitude. The uniformity of the spectra on top of the island also confirmed the atomic scale uniformity of the island.

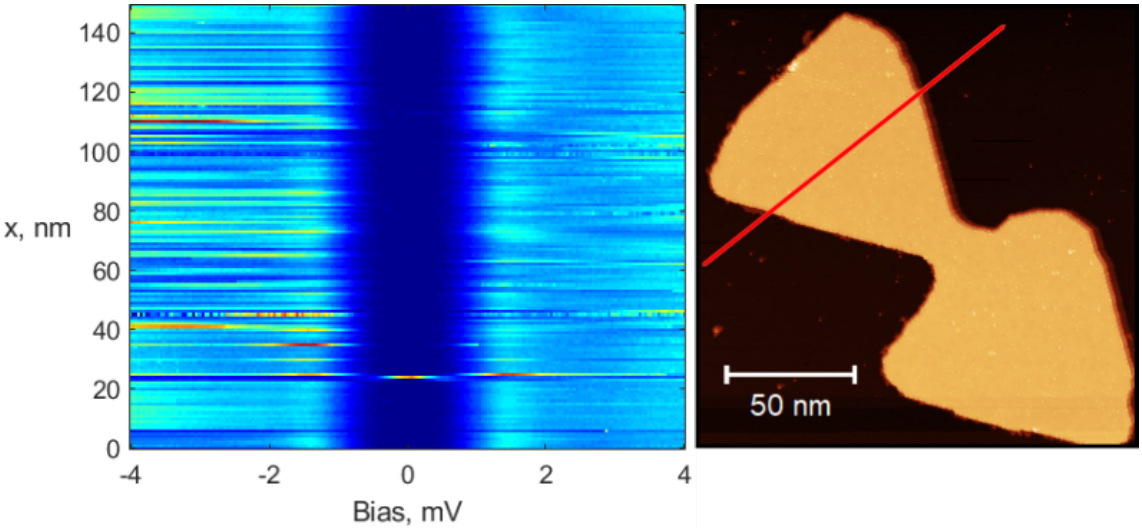

Figure 23: Line spectrum along the red line in the large area scan of an island. Modulation voltage 0.2 mV in the spectra, scan bias 1 V, current 20 pA. The zero bias excitation at 25 nm is located almost 10 nm away from the island edge. It did not reappear in the following spectra, which means it was probably caused by a tip event. Scan and spectra measured on sample D at 300 mK temperature.

Further evidence against ferromagnetic order in the islands with a 4.3 Å lattice constant was obtained by performing spectroscopy in an applied magnetic field. As shown in figure 24, the Abrikosov vortices induced by the magnetic field were largely unperturbed in proximity of the islands, suggesting their influence on the local magnetic field was negligible. The vortices were prone to move during scans and spectroscopy.

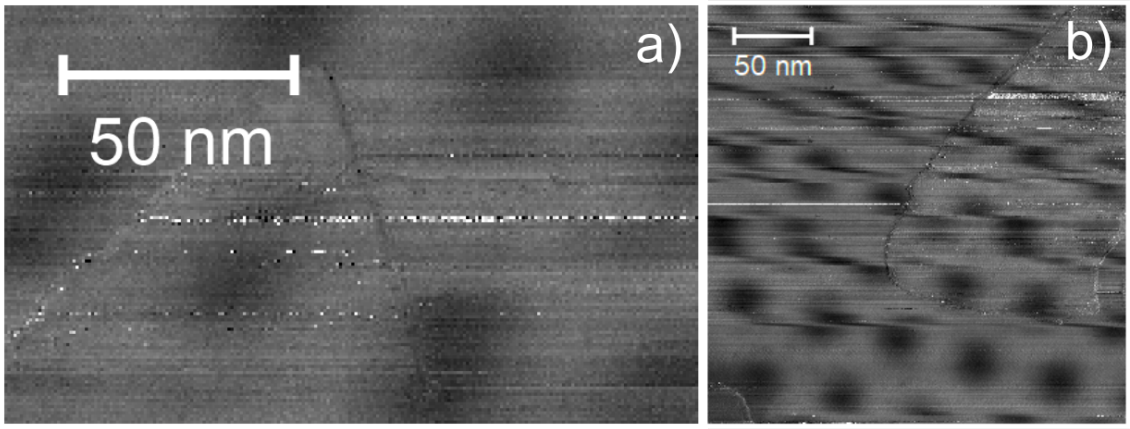

Figure 24: Lock-in amplified dI/dV maps of islands on sample D. **a)** Bias 15 mV, current 50 pA, applied magnetic field −1 T, temperature 2 K. **b)** Bias −20 mV, current 50 pA, applied magnetic field strength 1 T, temperature 300 mK. The Abrikosov vortices are largely unaffected by the presence of the islands, although they are easily moved by the STM tip.

Figure 25 shows a topologically trivial zero-bias conductance peak in a vortex core on sample D. The peak splits into two bias-symmetric quasiparticle states close to the vortex core before disappearing outside the vortex. The spectroscopy measurements taken in applied magnetic fields exhibited an oscillation of the superconducting gap width over a 2 nm length scale. This length scale does not directly correspond to the in-plane or out-of-plane coherence lengths of bulk $NbSe_2$ (7.8 nm and 2.8 nm, respectively [91, 92]).

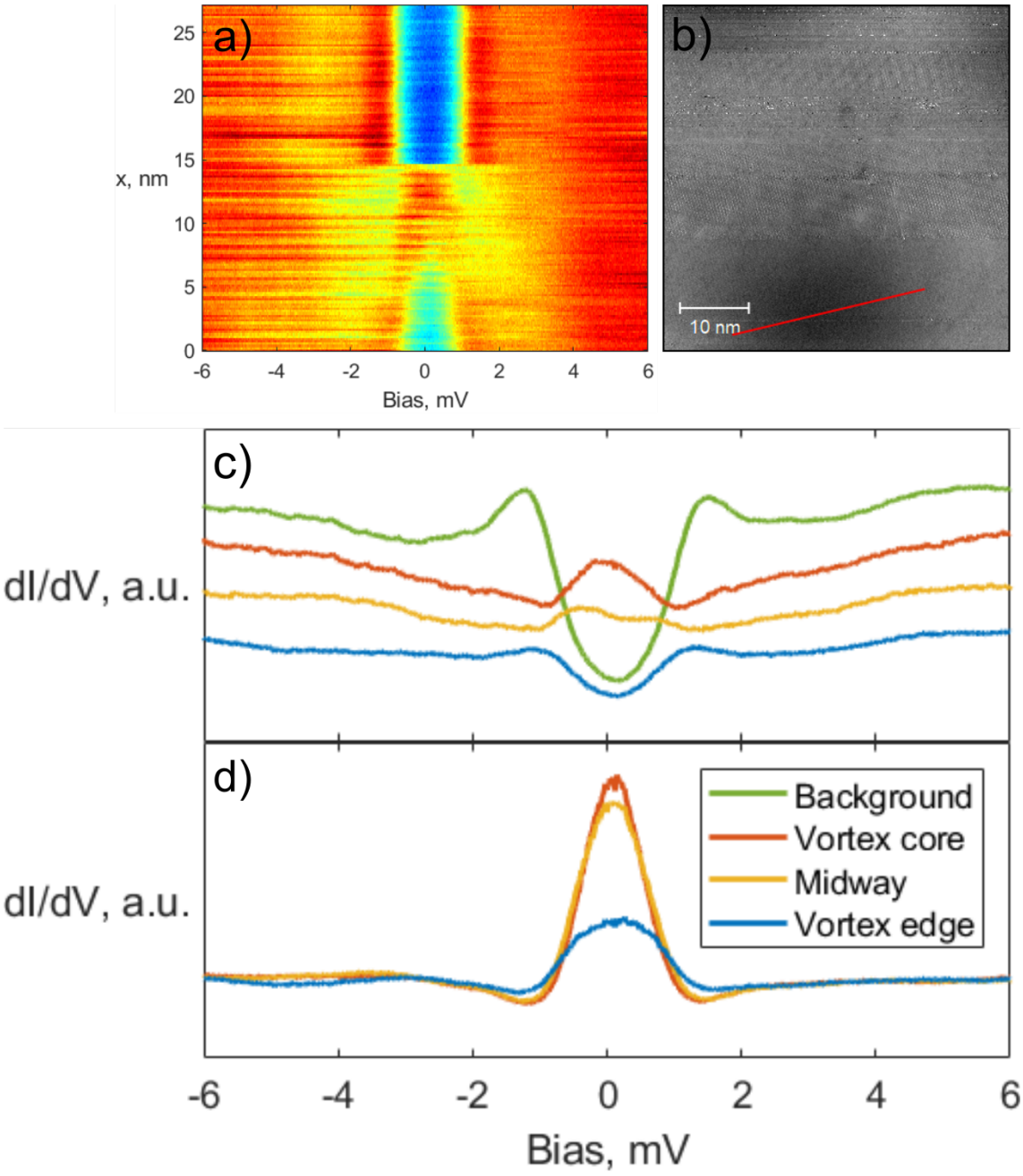

Figure 25: Line spectroscopy of an Abrikosov vortex core over a MnSe island on sample D. **a)** Line spectra along the red line shown in b). At 15 nm the vortex moved away from the scan line, exposing the background spectrum on the island. Voltage modulation 0.2 mV, colour scale normalized by current signal at 6 mV. **b)** Lock-in amplified dI/dV map. Bias 100 mV, current 500 pA. **c)** Averaged spectra from a) at different parts of the line. Spectra in the vortex are averaged over 10 spectra, the background spectrum is averaged over 70 spectra. **d)** Spectra in c) normalized with the averaged background spectrum. The measurements were performed in 1 T applied magnetic field and 300 mK temperature.

Despite the general lack of evidence for non-trivial topology and 2D magnetism, wide energy range spectra were averaged for eventual comparison against simulated band structure data. As shown in figure 26, the spectral features especially in the negative bias regime are dominated by the surface features. A background removal by dividing the spectra reveal bias-asymmetric features, a local minimum at around 100 mV and a shoulder-like feature at 200 mV.

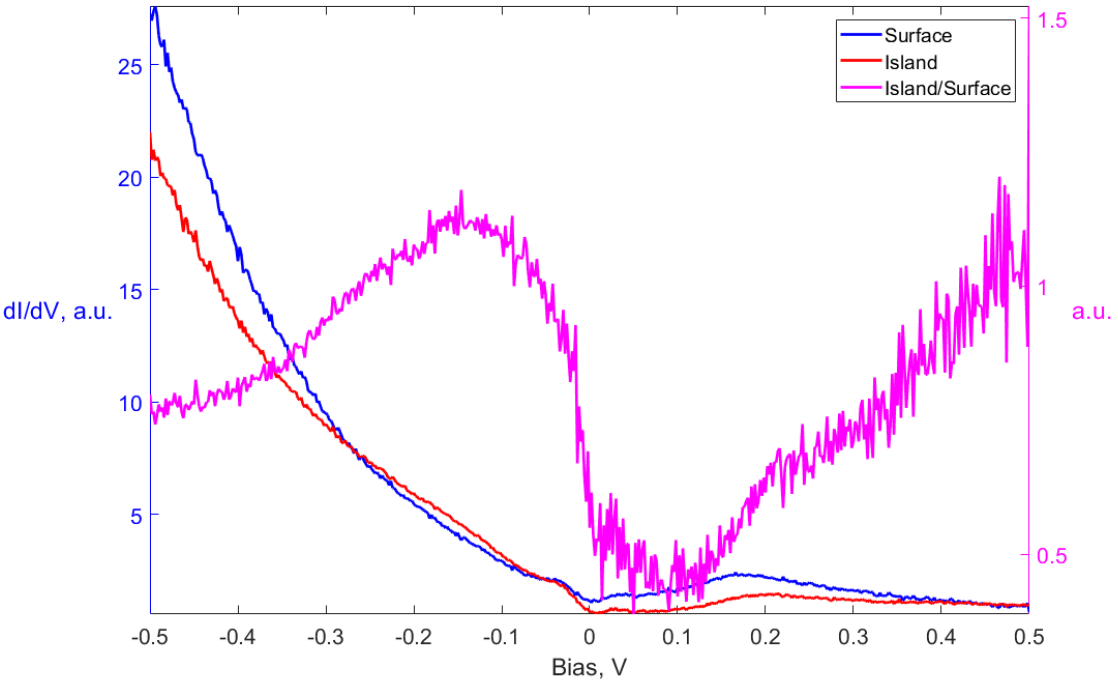

Figure 26: Large energy range spectra on top of a MnSe island and the $NbSe_2$ surface of sample D. The island and surface spectra are normalized to the positive bias ends of the curves. Note that the magenta-coloured curve corresponds to the right-hand side y-axis. The spectra were measured at 300 mK.

5 Summary and outlook

Manganese selenide/diselenide islands were grown on a niobium diselenide substrate. One particular sample exhibited signs of several phases of MnSe and possibly $MnSe_2$. The islands were successfully grown with several combinations of growth parameters, indicating that the conditions required for island formation are not insurmountably specific. The opposite conclusion was reached for growth on HOPG: no island formation was observed in any of the attempted growth conditions. Reasons for this difference can be speculated by analysing the effects of strain and the reaction paths of the $MnSe_x$ island formation. One possibility is that island formation requires nucleation centers or precursors with a non-vdW bond to the substrate: such a strong coupling could be influenced by the lattice constant mismatch between $MnSe_x$ and graphite.

STM was used to analyze the atomic scale topography of the sample surfaces. Four distinct populations of lattice constants could be identified from the samples: a 3.4 Å phase corresponding to $NbSe_2$ at various levels of intercalation, a 3.6 Å corresponding to $MnSe_2$ or intercalated $NbSe_2$, a 3.8 Å phase observed in a single high-coverage sample and finally a $4.2 - 4.5$ Å phase of MnSe islands. The apparent island heights obtained from the topography data averaged at ~ 5.5 Å (see appendix B for histograms of lattice constants and island heights). STM topography measured at 300 mK temperature revealed moiré patterns on the islands, with impurity atoms preferring adsorption sites coinciding with the pattern.

STS was performed on the successfully grown samples to investigate possible traces of magnetic order and non-trivial topological behaviour. Despite reasonable expectations, no edge states or zero bias conductance modes were observed in any of the samples. This cannot be explained with experimental limitations alone, since the island edges were atomically sharp and the spectroscopic energy resolution was maximised by cooling the sample to 300 mK. Moreover, zero bias conductance mapping showed that Abrikosov vortices induced by an applied magnetic field were unaffected by the islands: this would indicate that the islands had negligible effect on the local magnetic field on the surface. On the other hand, the superconducting gap on the previously mentioned high coverage sample appeared to magnify when measured on a secondary island layer. This tentatively indicates that the 3.8 Å phase might host magnetic phenomena, but unfortunately this phase could not be reproduced in subsequent samples.

Various further experiments and improvements can be suggested based on the obtained results. Firstly, the growth conditions and mechanisms could be investigated more thoroughly with an improved MBE setup. Adding a flux monitor into the selenium evaporator would give more accurate estimates of the relative fluxes of manganese and selenium. A cracker cell would make sure that the selenium comes out as individual atoms as opposed clusters of unknown sizes (a mass spectrometer could be utilized to analyze the cluster size distribution of the selenium flux with or without the cracker). Verifying and controlling Mn intercalation would enable investigations of various intercalation compounds [88]. Cleaving the $NbSe_2$ substrates without breaking the UHV conditions could also result in cleaner samples. These additions

could have substantial impacts on the reliability of $MnSe_2$ growth, and would also enable more controlled growth studies on HOPG and other substrates of interest. Measurement techniques like X-ray photoemission spectroscopy and magneto-optic Kerr effect systems could also be applied to access the average chemical and magnetic properties of the samples.

Modelling the MnSe and $MnSe_2$ islands on a $NbSe_2$ substrate with density functional theory and other methods would be instrumental in interpreting the obtained results. For instance, the island heights obtained in the topography measurements can correspond to either free-standing vdW monolayers or a five-layer complex with a Se-Nb-Se-Mn-Se stacking. Comparing the simulated properties of these compounds and their different structural phases to the obtained experimental data would provide deeper insight into the magnetic properties of the islands. Further research may reveal new ways to realize topological behaviour in these systems.

References

[1] V. L. Berezinskiĭ, "Destruction of long range order in one-dimensional and two-dimensional systems having a continuous symmetry group. I. Classical systems," *Sov. Phys. JETP*, vol. 32, pp. 493–500, 1971. [Zh. Eksp. Teor. Fiz.59,907(1971)].

[2] J. M. Kosterlitz and D. J. Thouless, "Ordering, metastability and phase transitions in two-dimensional systems," *Journal of Physics C: Solid State Physics*, vol. 6, pp. 1181–1203, apr 1973.

[3] X.-G. Wen, "Choreographed entanglement dances: Topological states of quantum matter," *Science*, vol. 363, no. 6429, 2019.

[4] S. R. Lee, P. A. Sharma, A. L. Lima-Sharma, W. Pan, and T. M. Nenoff, "Topological Quantum Materials for Realizing Majorana Quasiparticles," *Chemistry of Materials*, vol. 31, no. 1, pp. 26–51, 2019.

[5] M. Bonilla, S. Kolekar, Y. Ma, H. C. Diaz, V. Kalappattil, R. Das, T. Eggers, H. R. Gutierrez, M.-H. Phan, and M. Batzill, "Strong room-temperature ferromagnetism in VSe2 monolayers on van der Waals substrates," *Nature Nanotechnology*, vol. 13, no. 4, pp. 289–293, 2018.

[6] L. D. Landau, "On the theory of phase transitions," *Zh. Eksp. Teor. Fiz.*, vol. 7, pp. 19–32, 1937. [Ukr. J. Phys.53,25(2008)].

[7] S. Rao, "Introduction to abelian and non-abelian anyons," *arXiv e-prints*, p. arXiv:1610.09260, Oct 2016.

[8] A. Kitaev, "Fault-tolerant quantum computation by anyons," *Annals of Physics*, vol. 303, no. 1, pp. 2 – 30, 2003.

[9] P. W. Shor, "Fault-tolerant quantum computation," in *Proceedings of 37th Conference on Foundations of Computer Science*, pp. 56–65, Oct 1996.

[10] H. Weng, R. Yu, X. Hu, X. Dai, and Z. Fang, "Quantum anomalous Hall effect and related topological electronic states," *Advances in Physics*, vol. 64, pp. 227–282, May 2015.

[11] I. Pohjavirta, "2D metal-organic framework of dicyanoanthracene on Au(111)," master's thesis, Aalto University School of Science, 2019-03-12.

[12] S. Chern, "On the Curvatura Integra in a Riemannian Manifold," *Annals of Mathematics*, vol. 46, no. 4, pp. 674–684, 1945.

[13] D. A. Ivanov, "Non-Abelian Statistics of Half-Quantum Vortices in p-Wave Superconductors," *Phys. Rev. Lett.*, vol. 86, pp. 268–271, Jan 2001.

[14] Y. L. Chen, M. Kanou, Z. K. Liu, H. J. Zhang, J. A. Sobota, D. Leuenberger, S. K. Mo, B. Zhou, S.-L. Yang, P. S. Kirchmann, D. H. Lu, R. G. Moore, Z. Hussain, Z. X. Shen, X. L. Qi, and T. Sasagawa, "Discovery of a single topological Dirac fermion in the strong inversion asymmetric compound BiTeCl," *Nature Physics*, vol. 9, pp. 704–708, nov 2013.

[15] C. L. Kane and E. J. Mele, "Z_2 Topological Order and the Quantum Spin Hall Effect," *Phys. Rev. Lett.*, vol. 95, p. 146802, Sep 2005.

[16] M. Z. Hasan and C. L. Kane, "Colloquium: Topological insulators," *Rev. Mod. Phys.*, vol. 82, pp. 3045–3067, Nov 2010.

[17] A. Altland and M. R. Zirnbauer, "Nonstandard symmetry classes in mesoscopic normal-superconducting hybrid structures," *Phys. Rev. B*, vol. 55, pp. 1142–1161, Jan 1997.

[18] S. Ryu, A. P. Schnyder, A. Furusaki, and A. W. W. Ludwig, "Topological insulators and superconductors: tenfold way and dimensional hierarchy," *New Journal of Physics*, vol. 12, p. 065010, Jun 2010.

[19] É. Cartan, "Sur une classe remarquable d'espaces de Riemann, I," *Bulletin de la Société Mathématique de France*, vol. 54, pp. 214 – 216, 1926.

[20] A. P. Schnyder, S. Ryu, A. Furusaki, and A. W. W. Ludwig, "Classification of topological insulators and superconductors in three spatial dimensions," *Phys. Rev. B*, vol. 78, p. 195125, Nov 2008.

[21] M. Tinkham, *Introduction to Superconductivity*. Dover Publications, second ed., June 2004.

[22] W. Meissner and R. Ochsenfeld, "Ein neuer Effekt bei Eintritt der Supraleitfähigkeit," *Naturwissenschaften*, vol. 21, pp. 787–788, Nov 1933.

[23] Bednorz, J. G. and Müller, K. A., "Possible highTc superconductivity in the Ba-La-Cu-O system," *Zeitschrift für Physik B Condensed Matter*, vol. 64, pp. 189–193, Jun 1986.

[24] A. A. Abrikosov, "On the Magnetic properties of superconductors of the second group," *Sov. Phys. JETP*, vol. 5, pp. 1174–1182, 1957. [Zh. Eksp. Teor. Fiz.32,1442(1957)].

[25] F. London, H. London, and F. A. Lindemann, "The electromagnetic equations of the supraconductor," *Proceedings of the Royal Society of London. Series A - Mathematical and Physical Sciences*, vol. 149, no. 866, pp. 71–88, 1935.

[26] V. Eltsov, "Theory of Superconductivity." https://mycourses.aalto.fi/course/view.php?id=2226 Jan 2019. Course material for PHYS-0551 Low Temperature Physics V: Theory of Superconductivity.

[27] M. Cyrot, "Ginzburg-Landau theory for superconductors," *Reports on Progress in Physics*, vol. 36, pp. 103–158, feb 1973.

[28] R. Holm and W. Meissner, "Messungen mit Hilfe von flüssigem Helium. XIII. Kontaktwiderstand zwischen Supraleitern und Nichtsupraleitern," *Zeitschrift für Physik*, vol. 74, pp. 715–735, Nov 1932.

[29] J. Clarke, "The proximity effect between superconducting and normal thin films in zero field," *Le Journal de Physique Colloques*, vol. 29, no. C2, pp. C2–3, 1968.

[30] T. Nakamura, L. D. Anh, Y. Hashimoto, S. Ohya, M. Tanaka, and S. Katsumoto, "Evidence for Spin-Triplet Electron Pairing in the Proximity-Induced Superconducting State of an Fe-Doped InAs Semiconductor," *Phys. Rev. Lett.*, vol. 122, p. 107001, Mar 2019.

[31] Y. Kalcheim, O. Millo, A. Di Bernardo, A. Pal, and J. W. A. Robinson, "Inverse proximity effect at superconductor-ferromagnet interfaces: Evidence for induced triplet pairing in the superconductor," *Phys. Rev. B*, vol. 92, p. 060501, Aug 2015.

[32] T. Nakamura, L. D. Anh, Y. Hashimoto, Y. Iwasaki, S. Ohya, M. Tanaka, and S. Katsumoto, "Proximity-Induced Superconductivity in a Ferromagnetic Semiconductor (In,Fe)As," *Journal of Physics: Conference Series*, vol. 969, p. 012036, mar 2018.

[33] A. I. Buzdin, "Proximity effects in superconductor-ferromagnet heterostructures," *Rev. Mod. Phys.*, vol. 77, pp. 935–976, Sep 2005.

[34] J. Bardeen, L. N. Cooper, and J. R. Schrieffer, "Theory of Superconductivity," *Phys. Rev.*, vol. 108, pp. 1175–1204, Dec 1957.

[35] N. N. Bogoliubov, "A NEW METHOD IN THE THEORY OF SUPERCONDUCTIVITY. 1.," *SOVIET PHYSICS JETP-USSR*, vol. 7, no. 1, pp. 41–46, 1958.

[36] P. de Gennes, *Superconductivity of metals and alloys*. Frontiers in physics, W.A. Benjamin, 1966.

[37] J. Röntynen, *Topological superconductivity in magnetic adatom lattices*. PhD thesis, Department of Applied Physics, Aalto University School of Science, Espoo, Finland, 2016.

[38] L. Yu, "BOUND STATE IN SUPERCONDUCTORS WITH PARAMAGNETIC IMPURITIES," *Acta Physica Sinica*, vol. 21, no. 1, p. 75, 1965.

[39] H. Shiba, "Classical Spins in Superconductors," *Progress of Theoretical Physics*, vol. 40, no. 3, pp. 435–451, 1968.

[40] A. Rusinov, "ON THE THEORY OF GAPLESS SUPERCONDUCTIVITY IN ALLOYS CONTAINING PARAMAGNETIC IMPURITIES," *Soviet Physics JETP*, 1969.

[41] S. Kezilebieke, M. Dvorak, T. Ojanen, and P. Liljeroth, "Coupled Yu–Shiba–Rusinov States in Molecular Dimers on NbSe2," *Nano Letters*, vol. 18, no. 4, pp. 2311–2315, 2018. PMID: 29533636.

[42] A. Yazdani, B. A. Jones, C. P. Lutz, M. F. Crommie, and D. M. Eigler, "Probing the local effects of magnetic impurities on superconductivity," *Science*, vol. 275, no. 5307, pp. 1767–1770, 1997.

[43] K. Pöyhönen, A. Weststrom, J. Röntynen, and T. Ojanen, "Majorana states in helical Shiba chains and ladders," *Phys. Rev. B*, vol. 89, p. 115109, Mar 2014.

[44] D. Sticlet and C. Morari, "Topological superconductivity from magnetic impurities on monolayer $NbSe_2$," *arXiv e-prints*, p. arXiv:1906.01922, Jun 2019.

[45] S. Nadj-Perge, I. K. Drozdov, J. Li, H. Chen, S. Jeon, J. Seo, A. H. MacDonald, B. A. Bernevig, and A. Yazdani, "Observation of Majorana fermions in ferromagnetic atomic chains on a superconductor," *Science*, vol. 346, no. 6209, pp. 602–607, 2014.

[46] E. Majorana, "Teoria simmetrica dell'elettrone e del positrone," *Il Nuovo Cimento (1924-1942)*, vol. 14, no. 4, p. 171, 1937.

[47] W. H. Furry, "Note on the Theory of the Neutral Particle," *Phys. Rev.*, vol. 54, pp. 56–67, Jul 1938.

[48] S. R. Elliott and M. Franz, "Colloquium: Majorana fermions in nuclear, particle, and solid-state physics," *Rev. Mod. Phys.*, vol. 87, pp. 137–163, Feb 2015.

[49] G. Moore and N. Read, "Nonabelions in the fractional quantum Hall effect," *Nuclear Physics B*, vol. 360, no. 2, pp. 362 – 396, 1991.

[50] A. Y. Kitaev, "Unpaired Majorana fermions in quantum wires," *Phys. Usp.*, vol. 44, no. 10S, pp. 131–136, 2001.

[51] L. Fu and C. L. Kane, "Superconducting Proximity Effect and Majorana Fermions at the Surface of a Topological Insulator," *Phys. Rev. Lett.*, vol. 100, p. 096407, Mar 2008.

[52] T.-P. Choy, J. M. Edge, A. R. Akhmerov, and C. W. J. Beenakker, "Majorana fermions emerging from magnetic nanoparticles on a superconductor without spin-orbit coupling," *Phys. Rev. B*, vol. 84, p. 195442, Nov 2011.

[53] J. Röntynen and T. Ojanen, "Topological Superconductivity and High Chern Numbers in 2D Ferromagnetic Shiba Lattices," *Phys. Rev. Lett.*, vol. 114, p. 236803, Jun 2015.

[54] J. Li, T. Neupert, Z. Wang, A. H. MacDonald, A. Yazdani, and B. A. Bernevig, "Two-dimensional chiral topological superconductivity in Shiba lattices," *Nature Communications*, vol. 7, pp. 12297 EP –, Jul 2016. Article.

[55] C.-X. Liu, J. D. Sau, and S. Das Sarma, "Distinguishing topological Majorana bound states from trivial Andreev bound states: Proposed tests through differential tunneling conductance spectroscopy," *Phys. Rev. B*, vol. 97, p. 214502, Jun 2018.

[56] K. T. Law, P. A. Lee, and T. K. Ng, "Majorana Fermion Induced Resonant Andreev Reflection," *Phys. Rev. Lett.*, vol. 103, p. 237001, Dec 2009.

[57] K. S. Novoselov, A. K. Geim, S. V. Morozov, D. Jiang, Y. Zhang, S. V. Dubonos, I. V. Grigorieva, and A. A. Firsov, "Electric Field Effect in Atomically Thin Carbon Films," *Science*, vol. 306, no. 5696, pp. 666–669, 2004.

[58] K. S. Burch, D. Mandrus, and J.-G. Park, "Magnetism in two-dimensional van der Waals materials," *Nature*, vol. 563, pp. 47–52, Nov 2018.

[59] L. Onsager, "Crystal Statistics. I. A Two-Dimensional Model with an Order-Disorder Transition," *Phys. Rev.*, vol. 65, pp. 117–149, Feb 1944.

[60] N. D. Mermin and H. Wagner, "Absence of Ferromagnetism or Antiferromagnetism in One- or Two-Dimensional Isotropic Heisenberg Models," *Phys. Rev. Lett.*, vol. 17, pp. 1133–1136, Nov 1966.

[61] M. Gibertini, M. Koperski, A. F. Morpurgo, and K. S. Novoselov, "Magnetic 2D materials and heterostructures," *Nature Nanotechnology*, vol. 14, pp. 408 – 419, May 2019.

[62] B. Huang, G. Clark, E. Navarro-Moratalla, D. R. Klein, R. Cheng, K. L. Seyler, D. Zhong, E. Schmidgall, M. A. McGuire, D. H. Cobden, W. Yao, D. Xiao, P. Jarillo-Herrero, and X. Xu, "Layer-dependent ferromagnetism in a van der Waals crystal down to the monolayer limit," *Nature*, vol. 546, pp. 270 – 273, Jun 2017.

[63] K. Premasiri and X. P. A. Gao, "Tuning spin–orbit coupling in 2D materials for spintronics: a topical review," *Journal of Physics: Condensed Matter*, vol. 31, p. 193001, mar 2019.

[64] M. A. McGuire, H. Dixit, V. R. Cooper, and B. C. Sales, "Coupling of Crystal Structure and Magnetism in the Layered, Ferromagnetic Insulator CrI_3," *Chemistry of Materials*, vol. 27, no. 2, pp. 612–620, 2015.

[65] D. Shcherbakov, P. Stepanov, D. Weber, Y. Wang, J. Hu, Y. Zhu, K. Watanabe, T. Taniguchi, Z. Mao, W. Windl, J. Goldberger, M. Bockrath, and C. N. Lau, "Raman Spectroscopy, Photocatalytic Degradation, and Stabilization of Atomically Thin Chromium Tri-iodide," *Nano Letters*, vol. 18, no. 7, pp. 4214–4219, 2018. PMID: 29863369.

[66] S. Manzeli, D. Ovchinnikov, D. Pasquier, O. V. Yazyev, and A. Kis, "2D transition metal dichalcogenides," *Nature Reviews Materials*, vol. 2, June 2017.

[67] N. Elliott, "The Crystal Structure of Manganese Diselenide and Manganese Ditelluride," *Journal of the American Chemical Society*, vol. 59, no. 10, pp. 1958–1962, 1937.

[68] T. J. Kim, S. Ryee, M. J. Han, and S. Choi, "Sub-room temperature ferromagnetism and its nature in VSe_2 monolayer," *arXiv e-prints*, p. arXiv:1907.04790, Jul 2019.

[69] A. O. Fumega and V. Pardo, "Absence of ferromagnetism in VSe2 caused by its charge density wave phase," *arXiv e-prints*, p. arXiv:1804.07102, Apr 2018.

[70] P. M. Coelho, K. Nguyen Cong, M. Bonilla, S. Kolekar, M.-H. Phan, J. Avila, M. C. Asensio, I. I. Oleynik, and M. Batzill, "Charge Density Wave State Suppresses Ferromagnetic Ordering in VSe2 Monolayers," *The Journal of Physical Chemistry C*, vol. 123, no. 22, pp. 14089–14096, 2019.

[71] D. J. O'Hara, T. Zhu, A. H. Trout, A. S. Ahmed, Y. K. Luo, C. H. Lee, M. R. Brenner, S. Rajan, J. A. Gupta, D. W. McComb, and R. K. Kawakami, "Room Temperature Intrinsic Ferromagnetism in Epitaxial Manganese Selenide Films in the Monolayer Limit," *Nano Letters*, vol. 18, no. 5, pp. 3125–3131, 2018. PMID: 29608316.

[72] M. Kan, S. Adhikari, and Q. Sun, "Ferromagnetism in MnX2 (X = S, Se) monolayers," *Phys. Chem. Chem. Phys.*, vol. 16, pp. 4990–4994, 2014.

[73] C. Ataca, H. Şahin, and S. Ciraci, "Stable, Single-Layer MX2 Transition-Metal Oxides and Dichalcogenides in a Honeycomb-Like Structure," *The Journal of Physical Chemistry C*, vol. 116, no. 16, pp. 8983–8999, 2012.

[74] K. Persson, "Materials Data on MnSe (SG:186) by Materials Project," 9 2016. An optional note.

[75] K. Persson, "Materials Data on MnSe (SG:129) by Materials Project," 5 2016. An optional note.

[76] K. Persson, "Materials Data on MnSe (SG:194) by Materials Project," 2 2015. An optional note.

[77] G. Binnig, H. Rohrer, C. Gerber, and E. Weibel, "Tunneling through a controllable vacuum gap," *Applied Physics Letters*, vol. 40, no. 2, pp. 178–180, 1982.

[78] B. E. Murphy, *The physico-chemical properties of fullerenes and porphyrin derivatives deposited on conducting surfaces.* PhD thesis, School of Physics, Trinity College, Dublin, Ireland, 2014.

[79] M. Schmid, "The Scanning Tunneling Microscope [IAP/TU Wien]." http://www.iap.tuwien.ac.at/www/surface/stm_gallery/stm_schematic. Accessed: 28.9.2018.

[80] M. Ternes, *Scanning tunneling spectroscopy at the single atom scale*. PhD thesis, Séction de Physique, École Polytechnique Fédérale De Lausanne, Lausanne, Switzerland, 2006. https://infoscience.epfl.ch/record/64356/files/EPFL_TH3465.pdf.

[81] J. Bardeen, "Tunnelling from a Many-Particle Point of View," *Phys. Rev. Lett.*, vol. 6, pp. 57–59, Jan 1961.

[82] J. Tersoff and D. R. Hamann, "Theory of the scanning tunneling microscope," *Phys. Rev. B*, vol. 31, pp. 805–813, Jan 1985.

[83] M. Henini, *Molecular Beam Epitaxy: From Research to Mass Production*. Elsevier Science, 2018.

[84] D. Nečas and P. Klapetek, "Gwyddion: an open-source software for SPM data analysis," *Central European Journal of Physics*, vol. 10, pp. 181–188, 2012.

[85] I. Horcas, R. Fernández, J. M. Gómez-Rodríguez, J. Colchero, J. Gómez-Herrero, and A. M. Baro, "WSXM: A software for scanning probe microscopy and a tool for nanotechnology," *Review of Scientific Instruments*, vol. 78, no. 1, p. 013705, 2007.

[86] M. Ruby, "SpectraFox: A free open-source data management and analysis tool for scanning probe microscopy and spectroscopy," *SoftwareX*, vol. 5, pp. 31 – 36, 2016.

[87] S. Kezilebieke, M. N. Huda, P. Dreher, I. Manninen, Y. Zhou, J. Sainio, R. Mansell, M. M. Ugeda, S. van Dijken, H.-P. Komsa, and P. Liljeroth, "Epitaxial VSe_2 Monolayers on Superconducting $NbSe_2$." Unpublished at 29.7.2019.

[88] D. Chung, "Graphite Intercalation Compounds," in *Reference Module in Materials Science and Materials Engineering*, Elsevier, 2016.

[89] U. Chatterjee, J. Zhao, M. Iavarone, R. Di Capua, J. P. Castellan, G. Karapetrov, C. D. Malliakas, M. G. Kanatzidis, H. Claus, J. P. C. Ruff, F. Weber, J. van Wezel, J. C. Campuzano, R. Osborn, M. Randeria, N. Trivedi, M. R. Norman, and S. Rosenkranz, "Emergence of coherence in the charge-density wave state of 2H-NbSe2," *Nature Communications*, vol. 6, pp. 6313 EP –, Feb 2015. Article.

[90] M. Yankowitz, J. Xue, D. Cormode, J. D. Sanchez-Yamagishi, K. Watanabe, T. Taniguchi, P. Jarillo-Herrero, P. Jacquod, and B. J. LeRoy, "Emergence of superlattice Dirac points in graphene on hexagonal boron nitride," *Nature Physics*, vol. 8, pp. 382 EP –, Mar 2012.

[91] T. Uchihashi, "Two-dimensional superconductors with atomic-scale thickness," *Superconductor Science and Technology*, vol. 30, p. 013002, nov 2016.

[92] X. Xi, Z. Wang, W. Zhao, J.-H. Park, K. T. Law, H. Berger, L. Forró, J. Shan, and K. F. Mak, "Ising pairing in superconducting $NbSe_2$ atomic layers," *Nature Physics*, vol. 12, pp. 139 EP –, Nov 2015.

A Moiré pattern analysis by FFT

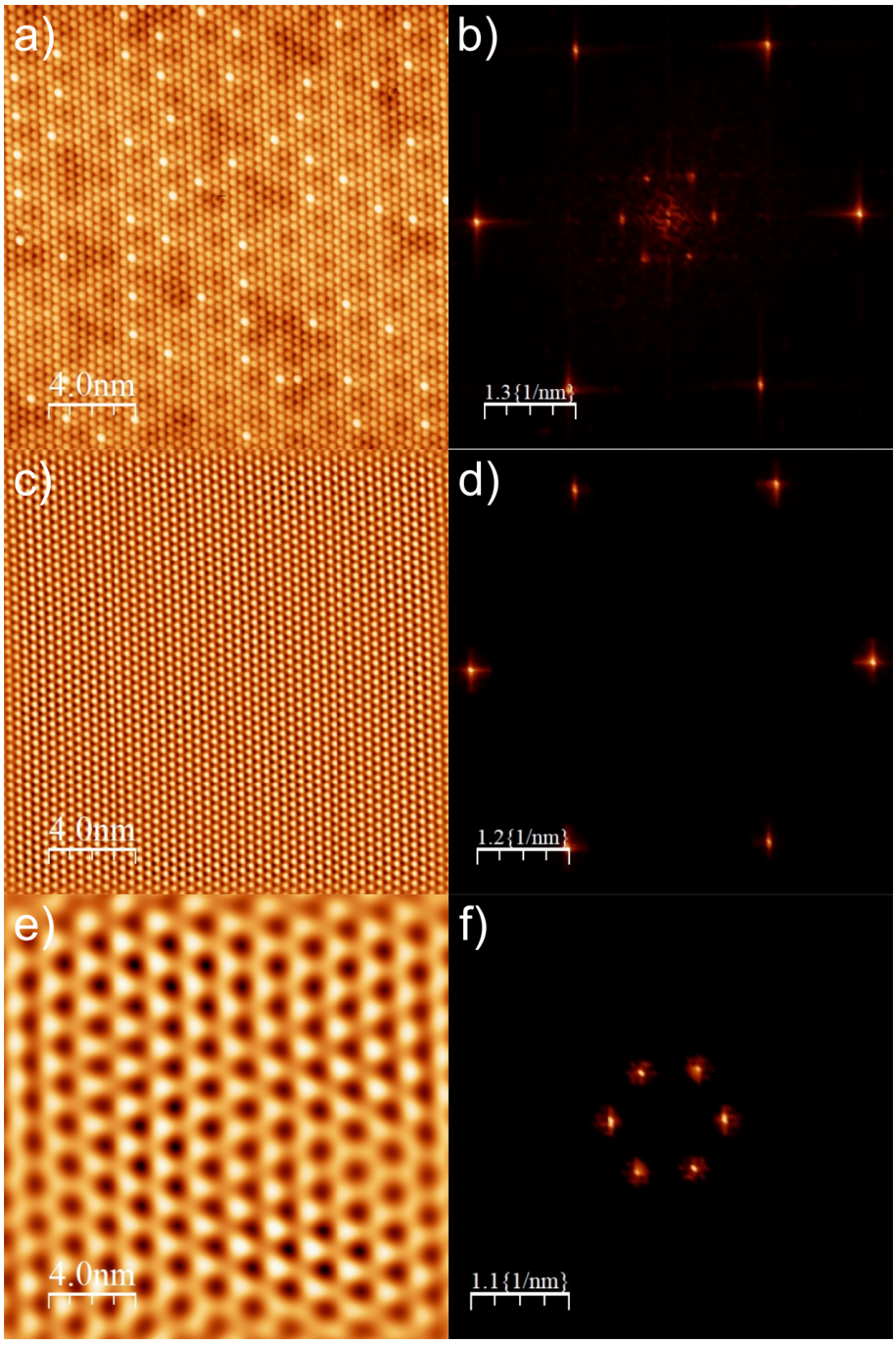

Figure A1: **a)** Original scan shown in figure 20. Bias 1 V, current 10 pA. **b)** Real part of the FFT of a). Two sets of Bragg peaks can be distinguished in addition to faint intensity maxima between them. **c)-d)** Fourier filtered lattice atoms with the corresponding Bragg peaks. **e)-f)** Fourier filtered moiré pattern with the corresponding Bragg peaks.

B Island height and lattice constant histograms

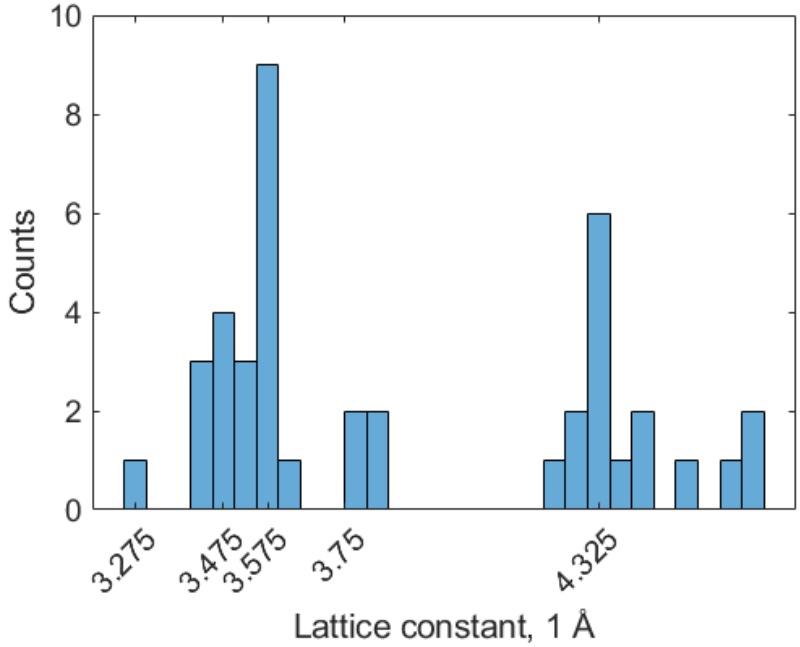

Figure B1: Histogram of the average lattice constants measured from atomic resolution STM scans. N = 41, bin width 0.05 Å.

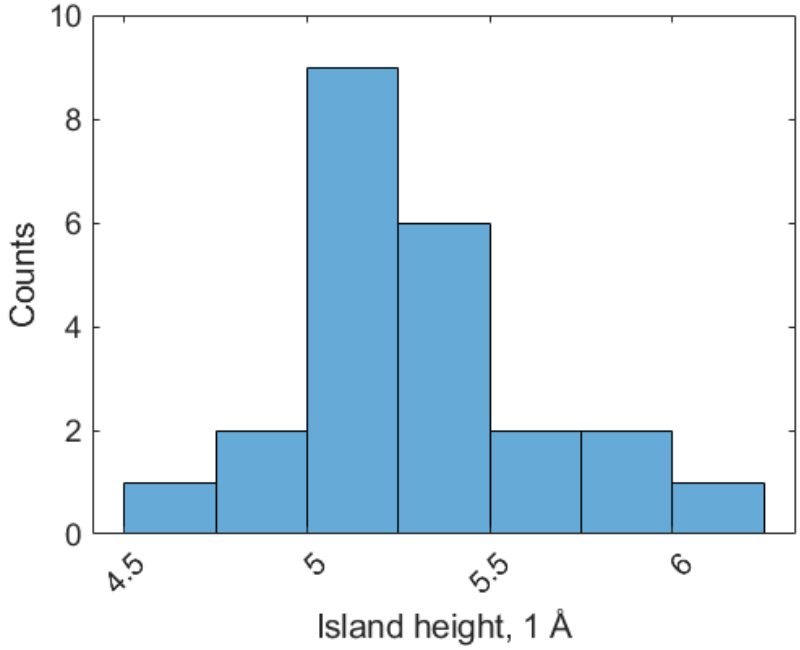

Figure B2: Histogram of the apparent island heights measured from large scale STM scans. N = 23, bin width 0.25 Å.